JGR Earth Surface

RESEARCH ARTICLE
10.1029/2023JF007093

The Impact of Extreme Rainstorms on Escarpment Morphology in Arid Areas: Insights From the Central Negev Desert

Yuval Shmilovitz[1], Francesco Marra[2,3], Yehouda Enzel[1], Efrat Morin[1], Moshe Armon[4], Ari Matmon[1], Amit Mushkin[5], Yoav Levi[6], Pavel Khain[6], Matthew W. Rossi[7], Greg Tucker[7,8], Joel Pederson[9], and Itai Haviv[10]

[1]The Fredy & Nadine Herrmann Institute of Earth Sciences, The Hebrew University of Jerusalem, Jerusalem, Israel, [2]Department of Geosciences, University of Padova, Padova, Italy, [3]National Research Council of Italy, Institute of Atmospheric Sciences and Climate (CNR-ISAC), Bologna, Italy, [4]Institute for Atmospheric and Climate Science, ETH Zurich, Zurich, Switzerland, [5]Geological Survey of Israel, Jerusalem, Israel, [6]Israel Meteorological Service, Beit Dagan, Israel, [7]Cooperative Institute for Research in Environmental Sciences (CIRES), University of Colorado Boulder, Boulder, CO, USA, [8]Department of Geological Sciences, University of Colorado Boulder, Boulder, CO, USA, [9]Geosciences Department, Utah State University, Logan, UT, USA, [10]Department of Earth and Environmental Sciences, Ben-Gurion University of the Negev, Beer-Sheva, Israel

Abstract The impact of climate on topography, which is a theme in landscape evolution studies, has been demonstrated, mostly, at mountain range scales and across climate zones. However, in drylands, spatiotemporal discontinuities of rainfall and the crucial role of extreme rainstorms raise questions and challenges in identifying climate properties that govern surface processes. Here, we combine methods to examine hyperarid escarpment sensitivity to storm-scale forcing. Using a high-resolution DEM and field measurements, we analyzed the topography of a 40-km-long escarpment in the Negev desert (Israel). We also used rainfall intensity data from a convection-permitting numerical weather model for storm-scale statistical analysis. We conducted hydrological simulations of synthetic rainstorms, revealing the frequency of sediment mobilization along the sub-cliff slopes. Results show that cliff gradients along the hyperarid escarpment increase systematically from the wetter (90 mm yr^{-1}) southwestern to the drier (45 mm yr^{-1}) northeastern sides. Also, sub-cliff slopes at the southwestern study site are longer and associated with milder gradients and coarser sediments. Storm-scale statistical analysis reveals a trend of increasing extreme (>10 years return-period) intensities toward the northeast site, opposite to the trend in mean annual rainfall. Hydrological simulations based on these statistics indicate a higher frequency of sediment mobilization in the northeast, which can explain the pronounced topographic differences between the sites. The variations in landscape and rainstorm properties across a relatively short distance highlight the sensitivity of arid landforms to extreme events.

Plain Language Summary Identifying the link between climatic properties and topography helps to elucidate key controlling processes affecting Earth's landscape evolution. In drylands, however, it is harder to associate topography with average climate as surface processes are significantly affected by spatially disconnected, discrete and short-duration rainstorms. In this study, we investigate whether variations in rainstorm properties can account for topographic differences along a 40-km-long hyperarid escarpment. Results indicate that in the drier parts of the escarpment, cliffs are steeper, and slopes are covered by finer sediment. Rainstorm statistical analysis indicates that the drier part of the escarpment is associated with extreme rainstorms characterized by higher rainfall intensities. We demonstrate that these storms mobilize sediment more frequently in the drier part of the escarpment, which can explain the pronounced topographic differences along the escarpment. This study presents a rarely-recognized link between small-scale variations in arid rainstorm properties and topography and highlights the susceptibility of arid landscapes to extreme rainstorms.

Key Points:

- The morphology of cliffs and sub-cliff slopes varies significantly with rainfall along a 40-km hyperarid escarpment
- The observed morphologic variability is triggered primarily by differences in sediment mobilization frequencies on sub-cliff slopes
- Rainstorm properties in arid landscapes could change over relatively short distances and leave a significant geomorphic imprint

Supporting Information:

Supporting Information may be found in the online version of this article.

Correspondence to:

Y. Shmilovitz,
yuval.shmilovich@mail.huji.ac.il

Citation:

Shmilovitz, Y., Marra, F., Enzel, Y., Morin, E., Armon, M., Matmon, A., et al. (2023). The impact of extreme rainstorms on escarpment morphology in arid areas: Insights from the central Negev desert. *Journal of Geophysical Research: Earth Surface*, *128*, e2023JF007093. https://doi.org/10.1029/2023JF007093

Received 30 JAN 2023
Accepted 15 SEP 2023

Author Contributions:

Conceptualization: Yuval Shmilovitz, Francesco Marra, Yehouda Enzel, Efrat Morin, Moshe Armon, Ari Matmon, Amit Mushkin, Matthew W. Rossi, Greg Tucker, Joel Pederson, Itai Haviv
Data curation: Yoav Levi, Pavel Khain
Formal analysis: Francesco Marra, Yoav Levi, Pavel Khain
Investigation: Yuval Shmilovitz, Francesco Marra, Yehouda Enzel, Efrat Morin, Moshe Armon, Amit Mushkin, Matthew W. Rossi, Greg Tucker, Joel Pederson, Itai Haviv

1. Introduction

1.1. Climate-Topography Feedbacks

Earth's surface is shaped by the climate's influence on erosion processes (Garrels, 1983; Perron, 2017; Tucker & Slingerland, 1997), motivating the search for correlations and associations between climate proxies, sedimentation

Methodology: Yuval Shmilovitz, Francesco Marra, Moshe Armon, Ari Matmon, Itai Haviv
Software: Yoav Levi, Pavel Khain
Supervision: Yehouda Enzel, Efrat Morin, Itai Haviv
Validation: Yuval Shmilovitz, Matthew W. Rossi
Visualization: Yuval Shmilovitz, Ari Matmon, Joel Pederson, Itai Haviv
Writing – original draft: Yuval Shmilovitz, Yehouda Enzel, Efrat Morin, Moshe Armon, Ari Matmon, Amit Mushkin, Greg Tucker, Joel Pederson, Itai Haviv
Writing – review & editing: Yuval Shmilovitz, Francesco Marra, Yehouda Enzel, Efrat Morin, Moshe Armon, Ari Matmon, Amit Mushkin, Greg Tucker, Joel Pederson, Itai Haviv

rates, and erosion patterns over various spatiotemporal scales (Herman et al., 2013; Molnar & England, 1990; Peizhen et al., 2001; Zhang et al., 2001). Part of this is exploring links between topography and climatic gradients (e.g., gradients in temperature and rainfall). Correlations of this type have been recognized where pronounced gradients exist in mean daily to decadal climate properties, such as monthly or mean annual precipitation (Adams et al., 2020; Bookhagen & Strecker, 2012; Ferrier et al., 2013; Olen et al., 2015; Stark et al., 2010; Thomson et al., 2010). However, the connection between mean conditions (e.g., mean annual rainfall) and erosion rate is not always simple (Langbein & Schumm, 1958; Tucker & Bras, 2000; Yair, 1983; Yair & Lavee, 1985). In drylands (hyperarid to semi-arid regions), topography-rainfall interactions are complicated by substantial variability in heavy rainfall (Marra et al., 2017; Morin et al., 2020). The mean daily rainfall in drylands can be very close to zero, while rare, heavy rainstorms may discharge tens of mm of rainfall in less than 1 hour (Goldreich, 1994; Goodrich et al., 1995; Sharon & Kutiel, 1986). This highlights the concept that the average conditions at a given site may not be relevant to what drives surface processes. In particular, fundamental questions remain concerning the sensitivity of arid landscapes to spatiotemporal variations in precipitation at the scale of individual storms. In this research, we examine the morphology of arid cliffs and slopes along a ∼40 km escarpment and mechanistically test whether storm-scale spatial variations are reflected in topography considering that climate changes during the Quaternary may have an influence.

1.2. Rainfall Characteristics and Measurement Challenges in Arid Settings

The high variability of rainfall in arid landscapes is the outcome of the quasi-random appearance of convective rain cells and of the spatial and temporal properties of rainstorms (Nicholson, 2011; Schick, 1988; Segond et al., 2007; Sharon, 1972). The characteristics of convective rainstorms play an important role in infiltration, runoff generation, flow discontinuities, transmission losses, and sediment mobilization in drylands (Dunkerley, 2012, 2019; Rinat et al., 2018; Yair & Lavee, 1985; Yair & Raz-Yassif, 2004; Yakir & Morin, 2011; Zoccatelli et al., 2019). Studies have demonstrated that erosion processes in drylands could be more sensitive to the properties of extreme rainstorms than to the long-term mean rainfall (DiBiase & Whipple, 2011; Enzel et al., 2012; Schick, 1988; Smith et al., 2019). Even at a longer timescale of landscape evolution, changes in the frequency-magnitude of extreme rainstorms have been hypothesized to trigger substantial hydrogeomorphic changes in drylands (Boroda et al., 2011; Ely et al., 1993; Enzel et al., 2012; Miller et al., 2010).

Understanding the role of rainfall characteristics in arid landscape evolution requires high-resolution rainfall data. However, due to the convective nature of rainfall in arid areas and the limited number of available observations, detecting spatiotemporal gradients in rainfall is extremely difficult. Rain gauge networks can provide reliable estimation for specific locations, but are sparse in many arid regions and tend to miss important storm characteristics (Goodrich et al., 1995; Marra & Morin, 2018). Where such measurements do exist, their total time span is often too short to derive meaningful statistics of the heaviest storms (Morin, 2011). Hope for bridging this gap lies in radar precipitation estimates, which provide spatial information and are increasingly integrated in dryland studies (Armon et al., 2020; Marra & Morin, 2018; Morin & Gabella, 2007; Rinat et al., 2018; Zoccatelli et al., 2020). However, the accuracy of radar estimates is heavily influenced by several sources of error, depending on location and the gauged data used for calibration, which restricts its use in remote areas (Villarini & Krajewski, 2010; Villarini et al., 2008).

An alternative source of spatially-distributed rainfall "records" is represented by a high-resolution, numerical weather prediction (NWP) models (e.g., El-Samra et al., 2017; Rostkier-Edelstein et al., 2014). A major advantage of NWP simulations is that they are potentially continuous in time and their spatial extent is only limited by computational power. High-resolution weather models explicitly resolve the convective processes (convection-permitting models) responsible for a large portion of the precipitation during extreme rainstorms. However, estimates derived from NWP models can suffer from statistical bias, and the modeled convective cells are often incorrectly positioned with respect to the observations (e.g., Roberts, 2008). Thus, to make accurate predictions, it is recommended to incorporate data assimilation (e.g., Gustafsson et al., 2018) or probabilistic approaches (Vincendon et al., 2011) to correct the bias, while examining the data at finer scales of tens to hundreds of kilometers (e.g., Armon et al., 2020). Nevertheless, NWP models reproduce physical processes forced by real boundary conditions and are therefore expected to correctly reproduce the statistics of precipitation (e.g., Liu et al., 2017). Indeed, such models have been successfully employed for rainfall intensity and frequency (Ban et al., 2014; Ludwig & Hochman, 2021; Schär et al., 2016), including analyzing precipitation extremes in drylands (Armon et al., 2022; Dayan et al., 2021; Kunz et al., 2018; Liu et al., 2021; Rinat et al., 2021).

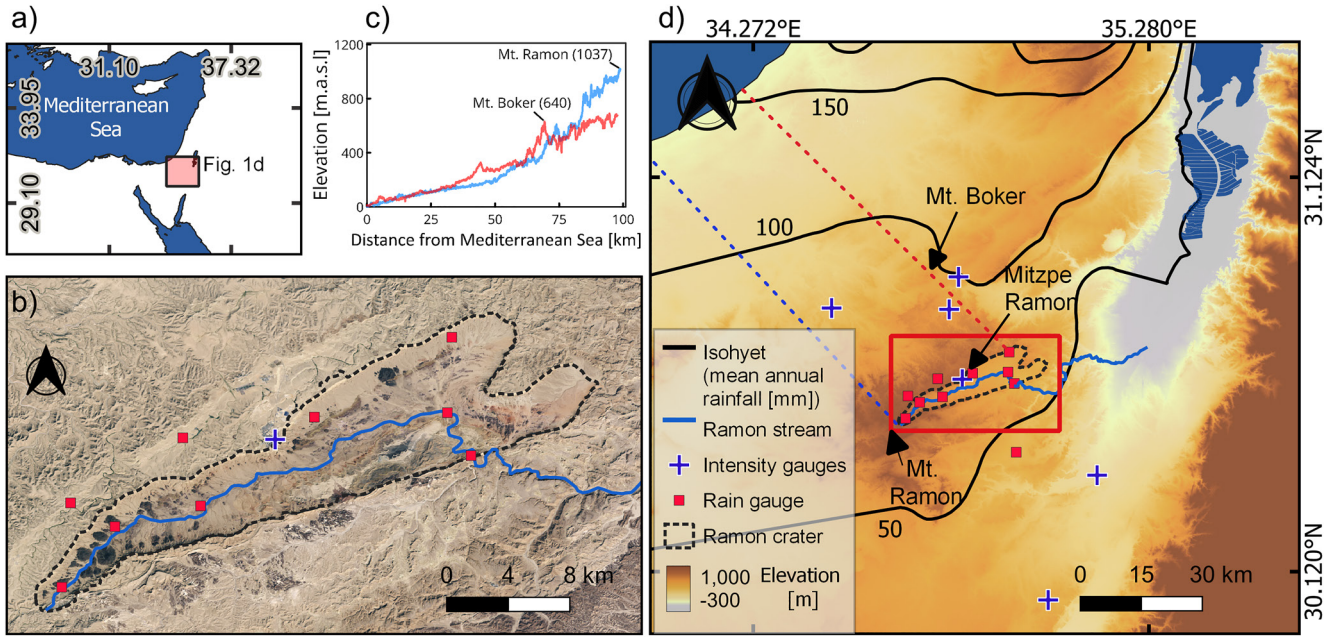

Figure 1. (a) Location of the study area. (b) Aerial photograph of the Ramon crater. The crater is outlined by a dashed line. (c) Topographic transects from the Mediterranean Sea to the southwestern and northeastern parts of the Ramon escarpment (transects locations are shown by dashed lines in panel (d). (d) Isohyets (black lines, in mm year^{-1}) of mean annual rainfall (IMS, 1980–2010) over the southern and central Negev (Israel).

1.3. Cliffs and Sub-Cliff Slope Morphology as Climatic Indicators

Escarpments are common in arid lands and are often characterized by cliff-forming hard rocks overlying more erodible layers. These erodible layers beneath the cliff are typically covered by a thin debris apron, composed of sediments produced by physical and chemical weathering processes operating on the cliff face, such as freeze-thaw cycles (Bruthans et al., 2017; Schumm & Chorley, 1966), salt weathering (Goudie et al., 1997; Pawlik, 2013) and differential thermal stress (Lamp et al., 2017). Sheet-flow is infrequent, but constitutes a dominant mechanism for the transport of sand and gravel-size material along the slopes (Michaelides & Martin, 2012; Parsons et al., 2009; Schmidt, 2009). It is generated mostly during high-intensity rainstorms when the infiltration rate is lower than the rainfall intensity.

A general hypothesis holds that alternating climate conditions could change the ratio between the rate of debris production from the cliff to the rate of breakdown and transport downslope. Under a scenario in which a sediment production is faster than debris evacuation, the cliff will be buried by its own debris (Selby, 1982), while enhanced debris removal promotes slope dissection, cliff undermining and the generation of talus slopes that become detached from the cliff (i.e., talus flatirons, Elorza & Martínez, 2001; Gerson, 1982; Schmidt, 1996). Several studies provide chronology that points to climatic variations as the first-order factor modulating the evolution of escarpments (Boroda et al., 2011; Elorza & Martínez, 2001; McCarroll et al., 2021). However, it remains unclear what kind of variations in climate properties would be needed to alter the sediment budget and lead to geomorphic changes, and at what spatiotemporal resolution such variations might operate.

Here, we investigate the cliffs and slopes of the Ramon erosional crater, located in the Negev desert (Figure 1). The northern rim of the crater is a ~40-km long escarpment, which has been forming since the Pliocene (Zilberman, 2000). Talus slopes and disconnected talus flatirons have developed below the cliffs as a result of climatic forcing, given no indication of significant tectonic activity in this area since the early Pleistocene. Thus, the Ramon escarpment is a natural experiment, where rainfall properties may differ along the cliff (Nativ & Mazor, 1987) and the coupling of rainfall and topography can be interrogated.

Our efforts address two fundamental questions: (a) How do cliff morphology and climate properties (primarily rainfall) change along an arid escarpment and over what spatiotemporal resolution? (b) Could the current spatial differences in climatic properties mechanistically account for observed morphologic variability? To answer these questions, we analyzed cliff and slope morphology using aerial LiDAR topography and field measurements of

sediment grain size. In addition, we characterized extreme, short-duration rainstorms based on sub-hourly rainfall data from a high-resolution NWP model and a novel statistical method. We used these data sets (field measurements, topographic data and rainfall statistics) to constrain a hydrologic model, which we used to predict surface runoff and the frequency of sediment mobilization along the slopes following synthetic storms. We thus quantify spatial changes in cliff morphology and rainstorm properties and examine whether the observed topographic differences can be mechanistically explained by the present-day rainstorm properties and erosion frequencies integrated over Quaternary timescales.

2. Geologic and Climatic Settings

2.1. Geology and Geomorphology

Ramon erosional crater (locally known as Makhtesh Ramon, in Hebrew) is situated along the crest of a NE-SW asymmetric anticline (Figure 1) and is the largest of three similar craters in the Negev desert. Despite its name, the crater was formed following tectonic folding and erosion and not due to an impact or volcanic activity. The Negev anticlines are part of the Syrian-Arc Fold Belt (SAFB; Krenkel, 1924), which started forming in the Early Senonian (Avni, 1991; Bentor & Vroman, 1952; Garfunkel, 1964) and were active at least until the Middle Miocene. The flanks of these asymmetric anticlines consist of a hard, Upper Cretaceous (Cenomanian-Turonian) sequence of mostly limestone and dolostone [Judea Group (Zilberman, 2000)], overlying much more erodible sandstone of Aptian age [Hatira Group (Zilberman, 2000)] (Figure 2). The resistant carbonate sequence has been eroded along the crests of the anticlines, exposing the erodible underlying sandstones (Zilberman, 2000) and forming a crest-parallel valley occupied by the Ramon drainage. Within the Ramon erosional crater, Early Cretaceous, Jurassic, and Triassic sandstone and dolostone are now exposed, capped by carbonate cliffs. This erosion occurred during the late Miocene or early Pliocene following the formation of the regional base level of the Dead Sea rift valley. A regional tilt down-to-the-east of the central Negev in the late Miocene and Pliocene is responsible for the higher elevation on the western side of the ∼40 km long and ∼12 km wide Ramon escarpment (Figures 1 and 2a). Since the early Pleistocene, there has been no indication of significant tectonic activity in this area. Along the northern rim of the escarpment are vertical and sub-vertical cliffs a few to tens of meters high, consisting of hard carbonate rocks and without significant spatial lithological differences. The outlet of the Ramon channel is located at 420 m above sea level, whereas Mount Ramon at the southwestern edge of the Ramon erosional crater is 1,037 m a.s.l (Figure 2a).

2.2. Climate

The Ramon erosional crater is located in the hyperarid Negev desert. Precipitation is characterized by discrete showers with extremely high inter-seasonal and annual variability and associated with three main synoptic-scale patterns: (a) Mediterranean cyclones (MC)—extratropical low-pressure systems routinely passing in wintertime through the eastern Mediterranean (Armon et al., 2018; Belachsen et al., 2017; Kahana et al., 2002), (b) Active Red Sea troughs (ARST) —surface pressure troughs extending from east Africa/Arabia toward the Red Sea that occasionally generates local, convective rain cells (Dayan & Morin, 2006; de Vries et al., 2013; Kahana et al., 2002), and (c) Tropical Plumes (TP)—rare synoptic type that produces relatively widespread and prolonged rainfall accompanied by a significant geomorphic response in large watersheds (Armon et al., 2018; Rubin et al., 2007; Yokochi et al., 2019).

Rain gauges able to measure short-duration intensities are sparse in this region, in some cases >50 km apart. Based on the Mitzpe Ramon station (Figure 1), situated on the northern rim of the Ramon cliffs, the mean annual rainfall is 70 mm (Israel Meteorological Service, IMS; 1980–2021). Approximately 65% of the rain falls during the winter (December–February), and 94% of the rainfall between October–March. Winter temperatures rarely reach freezing conditions (∼1 day in 2 years based on minimum daily temperature, IMS; 1980–2021), while in summer, the temperatures are often ≥30°C. The ephemeral Ramon stream is usually dry, with 2.5 floods occurring on average per year, with a maximum recorded peak discharge of 72 $m^3\ s^{-1}$ for the 250 km^2 Ramon watershed (Israeli Hydrological Service; 1982–2021). Thin Reg soils (Amit & Gerson, 1986) cover the slopes in the region and the rare vegetation is confined mainly to the channels.

3. Methods

3.1. Rainfall Data

Rain gauges and weather model simulations (Zängl et al., 2015) were used to characterize rainfall across the region and along the Ramon escarpment. Although the record from the weather model we use here is relatively

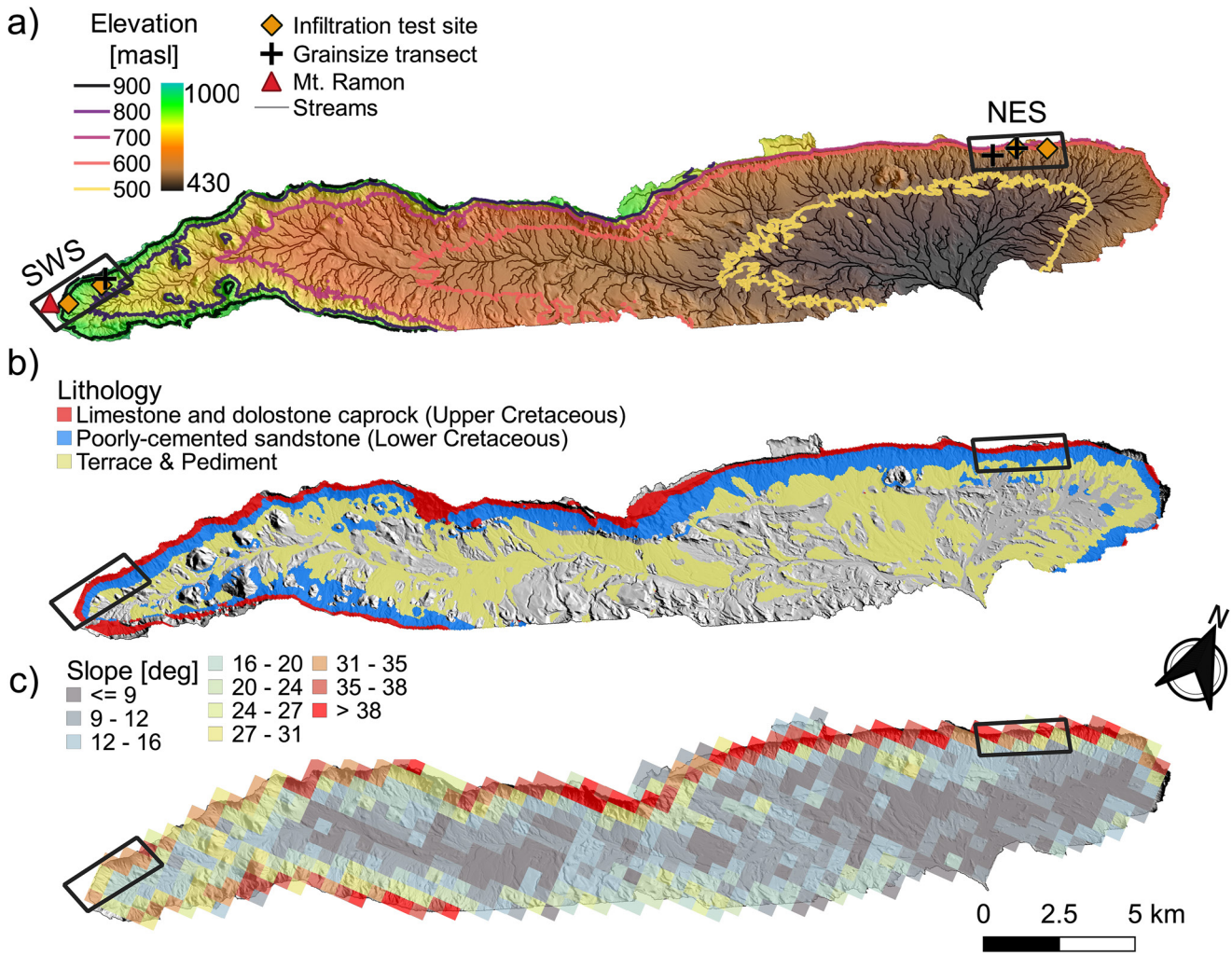

Figure 2. (a) Hillshaded map of the Ramon escarpment as derived from the aerial LiDAR survey (note the LiDAR extent does not cover the entire crater). Gray lines represent the drainage network. Black rectangles mark the western (SWS) and eastern (NES) sites. (b) Lithological map along the Ramon escarpment. (c) Gradients along the escarpment. LiDAR data were resampled with a 500 × 500 m^2 window (10^6 pixels) in (c) to better visualize the spatial pattern of the gradients. Gradient values presented are median window values.

short (8 years, see below), it provides unique spatial information on rainfall in this arid area, including explicit representation of convective processes that currently cannot be obtained by other instruments.

3.1.1. Rain Gauge Measurements

We used a combination of cumulative and intensity-recording rain gauges. Six intensity rain gauges with a 10-min temporal resolution are located 0–50 km from the escarpment and operated by the Israel Meteorological Service (IMS) (Figures 1b and 1d). The records of these gauges extend over 8–10 years between 2010 and 2020. Ten cumulative rain gauges 0–9 km from the escarpment (Figures 1b and 1d) with records extending over 4–5 years provide total rainstorm precipitation (i.e., they are measured once after each storm) and are operated by the Arava Drainage Authority. Both data sets were used to validate the weather model-derived rainfall record (see below), for both short (sub-hourly) and long (annual) durations.

3.1.2. Convection-Permitting Numerical Weather Prediction Model

We produced a gridded rainfall record for the Ramon region by the limited-area configuration of the ICOsahedral Non-hydrostatic (ICON) model (Zängl et al., 2015, for a further description regarding the ICON, see Text S1 in Supporting Information S1). Here we examine the effectiveness of the ICON rainfall products in the forecasting mode for rainfall analysis. We conducted simulations over the eastern Mediterranean domain of 25–39E/26–

36N (hereafter, ICON-IL) spanning the period between 01 September 2013 and 01 September 2021 (Khain et al., 2020). We initialized the simulations on a daily basis at 00 UTC and consisted of 78 hr forecast range. We used a convection-permitting resolution of ∼2.5 km with 65 vertical levels and an output temporal resolution of 10 min. We obtained initial and boundary conditions from the Integrated Forecasting System (IFS) model run by the European Center for Medium-Range Weather Forecasts (ECMWF) at a resolution of ∼9 km with 137 vertical levels. For each day, we used the forecast initialized at the beginning of the day (00 UTC) as the record for this day, that is, forecast lead times are 0–23 hr. We validated the ICON-IL rainfall against measured cumulative and intensity rainfall records in the region (see below).

3.2. Rainfall Statistical Analysis

We performed a pixel-based rainfall statistical analysis. In the first step, we calculated the mean annual rainfall and the maximum intensities for different durations for each model-based pixel. Then, we examined the frequency of sub-daily rainfall intensities to see if we could observe gradients in the rainfall intensities for different return levels, particularly during extreme events. We calculate sub-daily rainfall frequency using the Simplified Metastatistical Extreme Value approach (SMEV, Marra et al., 2019), a non-asymptotic statistical method based on the analysis of ordinary events, that are the independent realizations of the process of interest (details in Marra et al., 2020; Serinaldi et al., 2020). Considering the short record available (8 years) and the limited number of storms per year (∼10) in this region, this concept is more appropriate than traditional extreme value analysis methods for two reasons: (a) it facilitates the usage of all the available data as opposed to traditional methods that use one or two data points per year (Zorzetto et al., 2016); and (b) it explicitly considers the small number of storms per year in contrast with traditional extreme value theory, which assumes an infinite number of storms occurs every year (Fisher & Tippett, 1928). This method proved highly accurate in reproducing daily and sub-daily rain intensities corresponding to rare exceedance probabilities in the study region (Marra et al., 2020).

We calculate pixel-based return levels, which are the intensities corresponding to specific non-exceedance probabilities or return periods, for durations of 10, 20, 30, 60, and 120 min and for return periods (RPs) of 2,5,10,20,50, and 100 years. We adopted a bootstrapping procedure to overcome the stochastic sampling uncertainties due to the short record available (e.g., Goudenhoofdt et al., 2017). We randomly sampled (with replacement) 1,000 sets of 8-year-long intensity records from a 5 × 5 pixel window around the pixel of interest. We used these sets to estimate the SMEV distribution parameters and evaluate the rainfall intensities for all durations and return periods described above. Out of the 1,000 sets, we selected the 50th quantile (Q50) as the representative value for the pixel.

Following the method presented in Marra et al. (2020), we define storm-based ordinary events as wet intervals separated by >6 hr dry intervals. Ordinary events are then defined as the maximal intensities of each independent storm for the duration of interest. To quantify intensities associated with rare yearly exceedance probabilities, we explicitly consider their yearly occurrence frequency once the intensity distribution describing their tail is known (Zorzetto et al., 2016). We define the tail of ordinary events as the largest 45% events (i.e., events >0.55th percentile event), following the results in Marra et al. (2019). We used a stretched-exponential model (Weibull, as proposed by Wilson & Toumi, 2005 and confirmed by observations in the region by Marra et al., 2019; Marra et al., 2020; Marra et al., 2021a) to describe the tail, so that the yearly exceedance probability of extreme intensities could be written as

$$p(x;\lambda,k) = \left[1 - e^{-\left(\frac{x}{\lambda}\right)^k}\right]^n \quad (1)$$

where n is the yearly average number of storms, λ is the scale parameter and k is the shape parameter of the Weibull distribution. We computed the parameters of the tail for each duration by left-censoring the lowest 55% of the ordinary events and using least-squares regression in Weibull transformed coordinates. The codes used for the SMEV analyses are freely available (Marra et al., 2020). To validate the estimated parameters, we compare the calculated parameters with those derived from the available intensity gauges (Figure S1 in Supporting Information S1).

3.3. Topographic and Morphologic Analysis

We performed topographic and morphological analyses using a LiDAR-derived digital elevation model (DEM) of the Ramon escarpment, slopes, and channel network. The DEM has a pixel size of 0.5 × 0.5 m, with vertical

accuracy and effective precision of ±0.15 m and ±0.05 m, respectively. We focused our topographic analyses on selected sites along the southwestern and northeastern parts of the escarpment. We resampled the DEM of the study region to 1 × 1 m resolution for more efficient computation and used MATLAB TopoToolBox v2.0 (Schwanghart & Scherler, 2014) and QGIS (QGIS, 2019) to perform topographic analyses.

3.3.1. Cliff Gradient and Gully Density Along the Ramon Escarpment

We calculated the steepest descent slope and cumulative drainage area for each pixel using the 1 m DEM. We extracted stream networks using a drainage area threshold (10^4 m^2) based on breaks in the slope-area scaling and the locations of a few channel heads that were recognized in the field based on wash marks and bank morphology (Figure S2 in Supporting Information S1). After generating the stream network, we calculated the density of gullies beneath the cliff by counting the number of gully pixels (using the DEM) along lines spaced 10-m from each other and paralleling the cliff strike, across a band 150–350 m from the cliff top, which runs below the exposed bedrock cliff but above first-order stream confluences.

3.3.2. Geomorphic Analysis of the Southwestern and Northeastern Sites Along Ramon Escarpment

We analyzed two sites representing end members along the Ramon escarpment: a southwestern site (SWS) and a northeastern site (NES) lying 0–5 km and 30–35 km from Mount Ramon, respectively (Figure 2). At each of these sites, we mapped active talus slopes, talus flatirons (disconnected slopes) and pediment slopes (surfaces characterized by lower gradient, straighter longitudinal profiles, and smaller clasts relative to talus flatirons) according to surface and sedimentological characteristics. We constructed topographic profiles of active talus slopes perpendicular to the escarpment from the cliff top to a notable break in slope in the pediment or a streamline as the mean of >1,000 topographic lines perpendicular to the cliff, spaced 1-m apart.

In addition, we measured the b-axis size distribution of cliff-derived clasts at 10-cm intervals along two ∼20-m long transects parallel to the cliff and spaced 0.5 m apart at each of the SWS and NES sites (Wolman, 1954). In each of the transects, we randomly collected and measured ∼200 clasts (Neely & DiBiase, 2020; Shmilovitz et al., 2020, 2022; Verdian et al., 2021).

Finally, we measured infiltration characteristics and saturated hydraulic conductivity in the sub-cliff slopes using a tension infiltrometer (mini-disk, by METER environment) at each of the study areas. We conducted infiltration measurements at inter-rill areas at the lower part of the slope, with gradients ranging from 2° to 5°. We measured on a dry surface, at least 2 weeks after the last rainstorm to match the sparse number of precipitation events in a year in this region (15, on average at-a-point), which usually fall on a relatively dry surface. We applied a constant level of suction head to mitigate the effects of macropores on the infiltration and then recorded the volume of infiltrated water with time. The values of hydraulic conductivity (Ks) and sorptivity (S) were obtained from each infiltration time series using the method described by Zhang (1997).

3.4. Hydrological Modeling of Extreme Events

To evaluate the hydrologic and geomorphic responses of the slopes to rainstorms of different return periods, we applied hydrological simulations using synthetic storms, which were defined using intensity-duration-frequency relations. These storms were designed to represent specific frequencies of events and therefore enable us to simulate the hydrogeomorphic response under extreme rainstorms. We computed the storm intensities according to the alternating block method (Chow et al., 1988) for a total storm duration of 30 min (based on an average storm duration of ∼30 min measured in the Ramon station), in 10 min rain intensity segments, based on the SMEV frequency analysis (see above). We designed five storms for the SWS and NES (10 in total), corresponding to return periods of 2- (50%), 5- (20%), 10- (10%), 50- (2%), and 100-year (1%). For each of the storms, the maximum intensity for any duration represents the equivalent intensity according to the SMEV frequency analysis.

The hydrological model used is based on the Landlab toolkit (Barnhart et al., 2020; Hobley et al., 2017), an open-source Python library that facilitates building and modifying two-dimensional grid and process-based numerical models. A 2D grid of 1 × 1 m was created for the SWS and NES based on the characteristic longitudinal profile of the cliff and sub-cliff slope, with uniform topography running parallel to the cliff. The temporal resolution of the model is <1 min. In each storm simulation, we assume that rain falls on the grid uniformly and runoff generation is a function of the infiltration rate calculated by the Green-Ampt equation (Kidwell et al., 1997). Water propagation on the slope was described by a simplified inertial approximation of the shallow water equations,

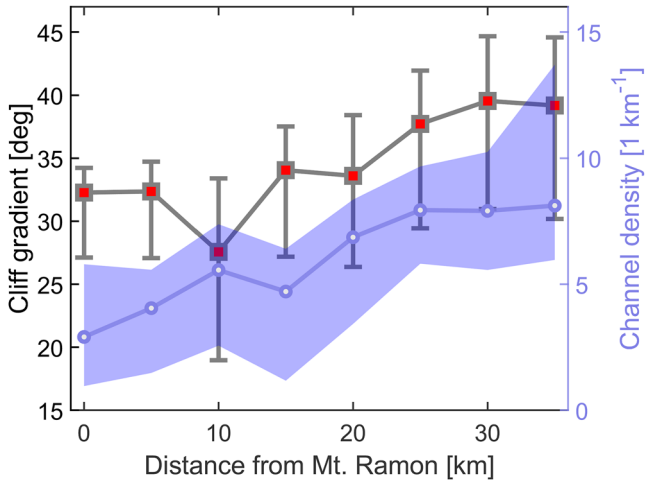

Figure 3. Cliff gradient (left axis, red squares) and density of colluvial channels (right axis, purple line) as a function of the distance eastward from Mount Ramon (location in Figures 1 and 2). The red squares represent the median gradient and the lower and limits of the upper gray lines represent the 25 and 75 quantiles, respectively (range of values from all the 0.5 × 0.5 m pixels within a 500 × 500 m^2 window). White dots and purple line represent median channel density and the shaded purple area represent the minimum and maximum densities for all calculated distances from the cliff.

following the solution of de Almeida et al. (2012) (for a full description of the hydrological model see Text S2 in Supporting Information S1). The basal shear stress $\tau_{i,t}\left[\frac{N}{m^2}\right]$, for each grid node i, at each simulation time step t, is determined by:

$$\tau_{i,t} = \rho \cdot g \cdot h_{i,t} \cdot S_i \quad (2)$$

where S_i is the gradient [m m^{-1}], $h_{i,t}$ is the water depth [m], ρ [kg m^{-3}] is the water density and g is gravitational acceleration [m s^{-2}]. The maximum shear stress $\tau_{\max,i}\left[\frac{N}{m^2}\right]$, per storm for each grid node i along the slope was converted to a critical transportable grain size $d_{c,i}$ [m] using Shields equation (Shields, 1936):

$$d_{c,i} = \frac{\tau_{\max,i}}{(\rho_s - \rho) \cdot g \cdot \tau_{c*}} \quad (3)$$

where ρ_s[kg m^{-3}] is the clast density and τ_{c*} is the critical Shields stress. We explore the range of transportable grain sizes, with the range chosen to represent uncertainty in the governing parameters including τ_{c*} ranges from 0.05 to 0.07 (Buffington & Montgomery, 1997; Shields, 1936), and Manning's n roughness coefficient. The latter is used in the water propagation algorithm and is considered here to range between 0.05 and 0.08 (Sadeh et al., 2018). In addition, we employ a range of hydraulic conductivities in the Green-Ampt equation based on the range of values from the infiltration tests at each site.

4. Results

4.1. Cliff and Talus Slope Morphology

The mean gradient of the cliffs along the Ramon escarpment increases systematically from southwest to northeast (Figures 2c and 3), with the mean gradient in the SWS [32.3° ± 0.01 (SE)] significantly lower (Wilcoxon rank-sum test, $p << 0.0001$) than the mean gradient at the NES [39.5° ± 0.01 (SE)]. Furthermore, the gradient along the SWS sub-cliff slopes is also lower (Figure S3 in Supporting Information S1), and these slopes are almost fully debris-mantled (Figure 4d). The characteristic slope profile in the west is longer (330 vs. 200 m in the east) (Figure 5a), and the SWS profiles are slightly less concave than the NES profiles, as indicated by their normalized profiles (Figure 5b).

Grain size decreases downslope at both sites (Figure 5c). The d_{50} at the SWS decreases from 60 mm at 50 m above the caprock base, to 31 mm at 160 m downslope. At the NES, the d_{50} decreases from 32 mm at 40 m above the caprock base, to 18 mm at 140 m downslope. For any given distance along the slope, the median grain size of cliff-derived sediment in the SWS is larger relative to the corresponding grain size in the NES. Large boulders (>1,000 mm) rarely appear at distances >100 m from the cliff face along the NES slopes. Conversely, in the SWS, large boulders are common at distances >100 m from the cliff (Figure 4d). Based on infiltration tests, the saturated hydraulic conductivity in both sites varies between 1 and 13 mm hr^{-1} (Table S1 in Supporting Information S1).

Talus flatirons, which are no longer connected to the cliff, cover 7% of the SWS area (between the cliff top and a parallel line in a distance of 400 m below), whereas in the NES they cover 12% (Figure S4 in Supporting Information S1). These relict slopes are separated from the cliff by gullies. A general increase in the density of gullies toward the NES is responsible for a more dissected landscape (Figures 3 and 5d; Figure S4 in Supporting Information S1).

4.2. The Spatial Distribution of Rainfall

4.2.1. Mean Annual Rainfall

The modeled (ICON-IL) annual rainfall amount matches the gauge-based rainfall (RMSD = 13.7 mm, Figure 6). The simulated regional pattern of mean annual rainfall decreases from north (~100 mm) to the south (<30 mm) as expected (Goldreich, 2003). Along the Ramon escarpment, it decreases by 37%–50% from 80 to 90 mm near Mount Ramon (the southwestern part of the escarpment) to 45–50 mm in the northeast.

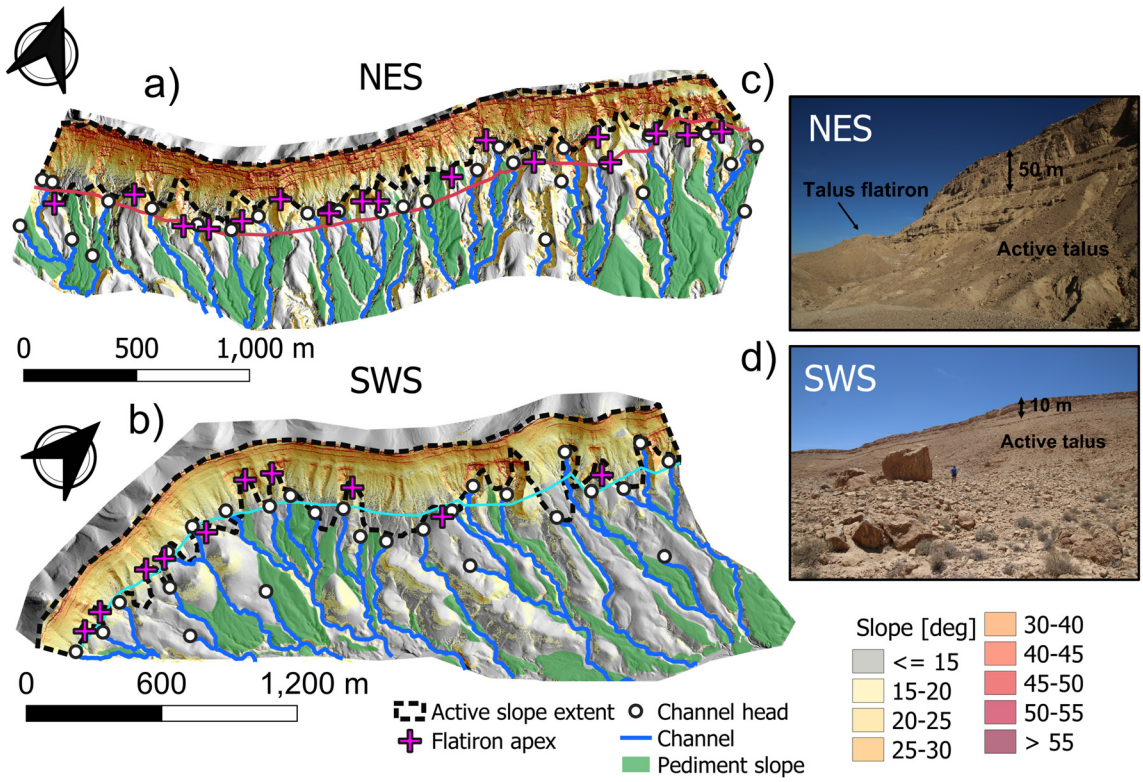

Figure 4. Topography and the main morphological units in the studied sites. (a, b) Hillshaded topography and slope maps of the NES and SWS, respectively. Red and cyan lines roughly paralleling the cliff strike, in (a and b), respectively, mark the locations of topographic transects shown in Figure 5d. (c, d) Representative photos of cliff and sub-cliff slopes in the NES and SWS, respectively.

4.2.2. Spatial Distribution of Rainfall Extremes

In order to verify that the ICON-IL produces realistic rainfall in the study area, we compare the exceedance probability (i.e., one minus the cumulative probability; Figure S5 in Supporting Information S1), from the ICON-IL model to the 10 min rainfall from intensity gauges. Over 75% of the observed frequency curves at high intensities of >12 mm hr^{-1} are within the range of the ICON-IL intensities. For low intensity (<6 mm hr^{-1}), the ICON-IL rainfall underestimates the frequency in comparison with all the gauge measurements. However, these differences are relatively small (note the log-log scale of Figure S5 in Supporting Information S1) and should have minor influence on surface processes driven by extreme events.

We utilized the SMEV method for each pixel of the ICON-IL record to derive spatial distributions of rain intensities for different return periods and durations (Figure 7). For a 2-year return period (Figure 7c), rainfall intensity in the region decreases from north to south in parallel to the spatial pattern of annual rainfall. At the SWS, the mean rain intensities for 10, 20, 30, 60, and 120 min are 19, 14, 11, 7, and 4 mm hr^{-1} respectively, similar to the NES intensities: 18, 14, 11, 7, and 4 mm hr^{-1}, respectively (Figure 7, based on 4 pixels within each of the domains). However, large differences between the sites emerge for longer return periods; specifically, the eastern and drier part of the escarpment is characterized by higher rain intensity (Figure 7d). For example, the mean rain intensities of a 100-year return period storm for 10, 20, 30, 60, and 120 min are 76, 53, 31, 25, 17 mm hr^{-1} for the SWS (Figures 7a, 7c, and 7e) and 100, 74, 56, 33, 21 mm hr^{-1} for the NES (Figures 7b, 7d and 7f).

4.3. Sediment Mobilization Under Storms of Different Return Periods

To link synthetic storm events to resultant erosion, overland flow events associated with storms of different return periods were modeled at the SWS (mean annual rainfall 70–90 [mm]) and NES (mean annual rainfall 45–55 [mm]). At both sites, the maximal transportable grain size along the slope shows a similar pattern (Figures 8c and 8d). The transportable grain size (based on the median values of the uncertainty range, see colored curves in Figures 8c and 8d) reaches a maximum at a distance of 100–150 m downslope, due to high gradients and high-enough water

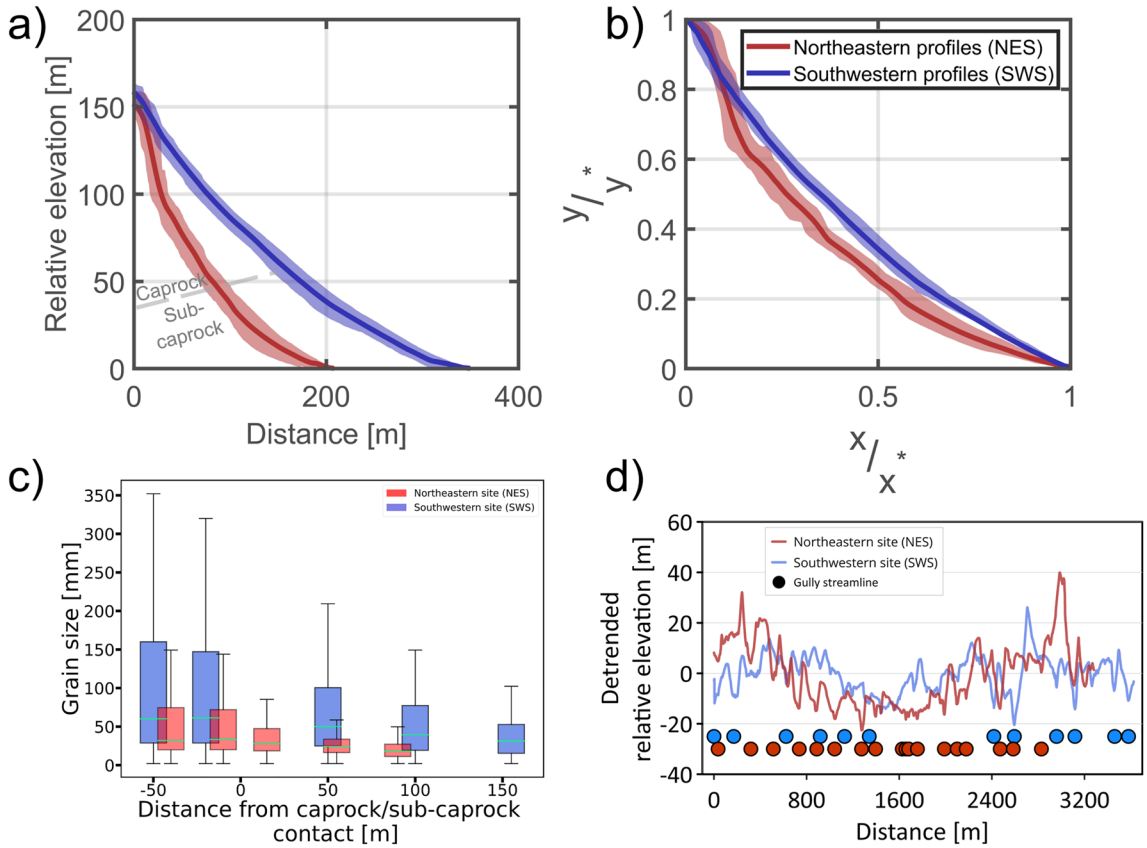

Figure 5. (a) Topographic profiles perpendicular to the cliff for the SWS (blue) and NES (red). (b) Topographic profiles normalized by total relief. (c) Measured grain size in the SWS and NES. The horizontal green line represents the 50 quantile (d_{50}) and the lower and upper box limits represent the 10 and 84 quantiles (d_{10}, d_{84}). (d) Detrended topographic transects along lines roughly paralleling the cliff strike (transect locations are shown by red and cyan lines in Figures 4a and 4b, respectively). Red and blue circles represent locations (x-axis only) of gully pixels along the NES and SWS transects, respectively.

levels (Figure 8). The smaller maximal transportable grain size in the uppermost parts of the slope results from the shallower flow depth. At the lowermost parts of the slope, the smaller maximal transportable grain size is controlled by the reduced topographic slope. For 2- and 5-year return period storms, the maximal transportable grain size in the NES is ~10 mm (Figure 8d). No runoff is generated in the SWS for the 5-year return period storm, indicating that the average frequency for runoff generation in the SWS is between 5 and 10 years, on average (Figures 8c and 8d).

Comparing the maximal transportable clast size and the measured clast size (d_{50}, gray circles) for >5-year return period storms show substantially different behavior between the SWS and the NES. In the SWS (wetter), the maximal transportable grain size computed for a 50-year storm do not exceed the measured clast size and for a 100-year storm, the maximum transportable grain sizes are larger than the measured clast sizes only at distances >200 m away from the cliff (Figure 8c). This indicates that sediment is relatively immobile in the SWS, being transported only under the most extreme modern storms (return period >50-year) at the lower parts of the slope. In contrast, hydrologic simulations indicate that the transportable clast sizes in the NES (drier) under the 100- and 50-year storms are larger than the measured clast sizes all the way from 50 to 200 m from the cliff. Based on our overland flow modeling, the frequency of large-grain mobilization in the NES is between once in 10 and once in 50 years (Figure 8d).

5. Discussion

5.1. Contrasting Climate of the Western and Eastern Ramon Escarpment

Across a distance of ~40 km along the Ramon escarpment, the mean annual rainfall decreases from ~90 mm in the southwestern part to ~45 mm in the northeastern part, confirming the pattern inferred from sparse, previous rainfall measurements (Nativ & Mazor, 1987). The rainfall in the area is dominated by Mediterranean

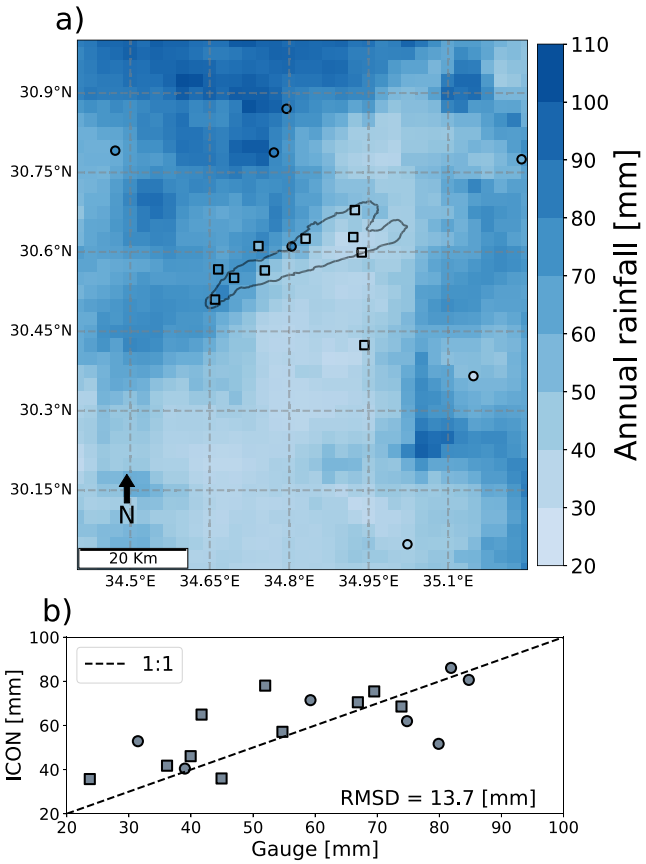

Figure 6. (a) Mean annual rainfall calculated using the ICON-IL record over the Ramon region (8-year). Colored circles and squares mark the locations of intensity and cumulative rain gauges, respectively. (b) Comparison of the mean annual rainfall derived from the gauges in (a) and the corresponding ICON-IL pixels.

cyclones (MCs), with >75% of rain days in the region associated with that synoptic pattern (Marra et al., 2021a, 2021b). Therefore, the broad spatial pattern in the annual rainfall must be related to the distance from the Mediterranean Sea, the distance from the storm track, and elevation/orography (Goldreich, 1994). However, since the escarpment roughly parallels both the Mediterranean coastline to the northwest (a distance of ∼100 km along the length of the crater rim) and is perpendicular to the general track of MCs (Alpert et al., 2016; Romem et al., 2007), the distance from the Mediterranean sea can be ruled out as an explanation for the smaller-scale rainfall gradient along this rim.

Most rain days in this region occur during the last stages of the passage of an MC, with winds veering to NW-NNW rather than SW-WNW at earlier stages (Armon et al., 2019). Precipitation during the later stages of an MC is commonly lighter and prolonged, conditions favorable for orographic enhancement (Enzel et al., 2008; Minder et al., 2015; Yuter & Houze, 1995). Orographic rainfall tends to have longer durations and lower rain intensity over short (<1 hr) durations, and higher intensity over long durations (>6 hr) (Marra et al., 2021b; Roe, 2004). Since the western part of the escarpment is ∼400 m higher than its eastern part, it produces more orographic rainfall, and indeed the western escarpment is the first major topographic rise encountered by air flowing from the sea. In contrast, the eastern side lies downwind from another mountain range (Mount Boker, Figure 1c). Therefore, passing from the sea to these inland sites, air can be drained out of moisture upwind of the eastern side of the escarpment. A greater orographic effect can increase the number of rain events as well as the rainfall intensity over the western site, particularly for long duration events. In fact, the western and eastern sites exhibit similar rainfall intensities for the 2-year return period and thus, the difference in the annual amounts is more likely due to differences in the number of storms per year (∼13 vs. ∼8 for the SWS and NES, respectively, Figure S1 in Supporting Information S1), a parameter that could be controlled by the orographic effect.

In contrast, the impact of orography on short-term, sub-daily extremes in this region is much less well understood. Marra et al. (2021a, 2021b) quantified the impact of orography on sub-daily precipitation extremes related to MCs by identifying a reverse orographic effect (Allamano et al., 2009; Avanzi et al., 2015; Formetta et al., 2022) in which rainfall intensity declines with increasing elevation for storm durations of 10–60 min. A decrease in the extreme tails with rising elevation was also recently recognized in the eastern Italian Alps (Formetta et al., 2022). These previous studies proposed that rainfall intensity decreases with elevation for longer durations because precipitation redistribution toward stratiform-like processes smooths the intensity structure within the storms. At the Ramon Escarpment, we document a reduction in the extreme intensities with elevation also for durations of 10–30 min.

In addition to MCs, ARSTs can also contribute to differences between rainfall intensities over the escarpment. Under ARST-borne storms, moisture is potentially supplied from other directions in addition to the Mediterranean Sea, namely from the Red Sea south of the study area or from the SW at the mid-upper troposphere (Armon et al., 2018). As a result, convective rainstorms develop (Ashbel, 1938), which potentially intensify with temperature; that is, they can be stronger specifically in the southern and eastern Negev, where temperatures are higher (Kahana et al., 2002). This is also in agreement with the higher correlation of rain days with ARST occurrences toward the southeastern Negev (Marra et al., 2020, 2021a, 2021b). The convective nature of precipitation during ARSTs, emphasizes the dominance of short-duration high-intensity rainfall. Thus, under ARST conditions, the northeastern part of the Ramon crater could experience higher extreme short-duration intensities relative to the southwestern part.

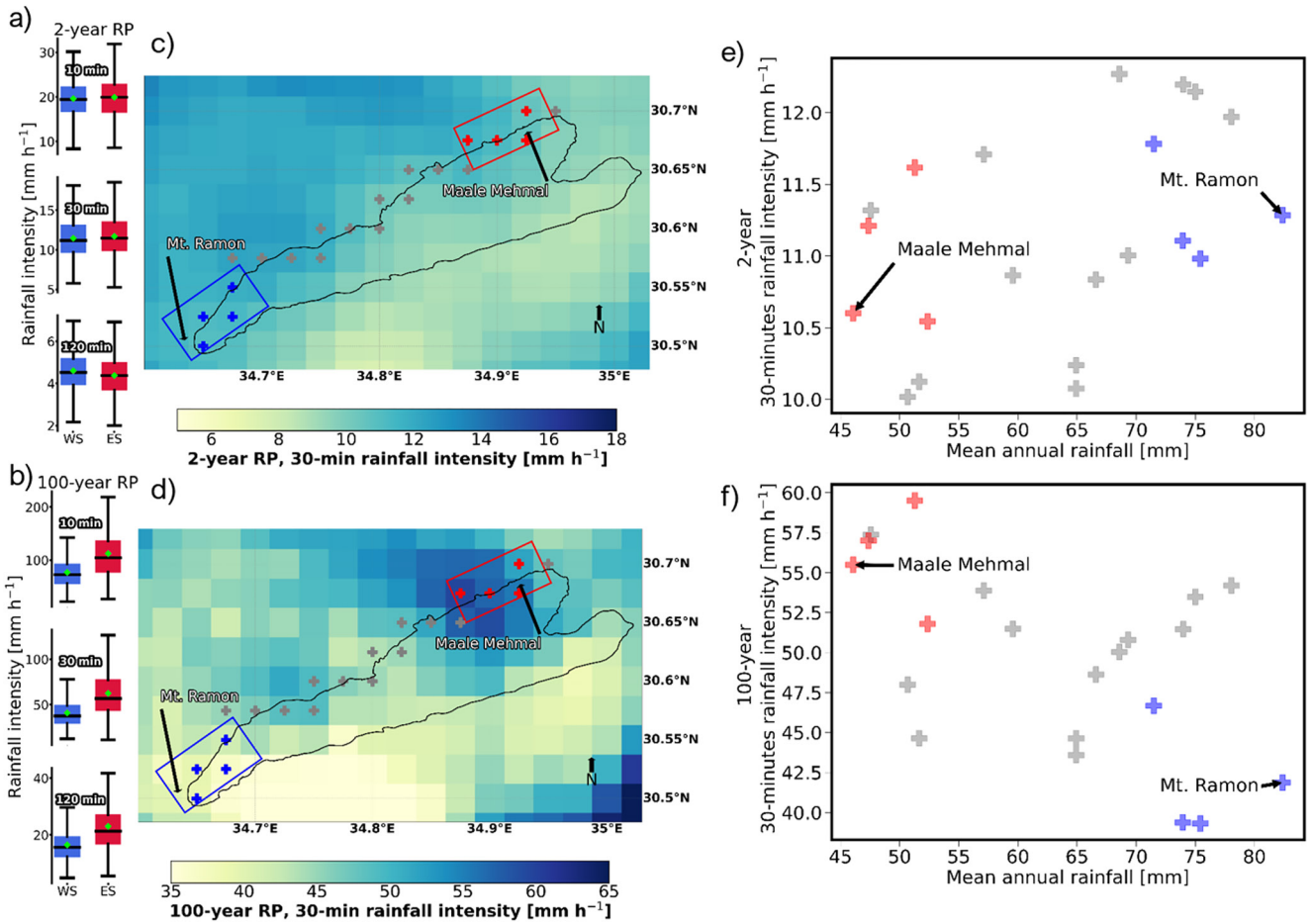

Figure 7. The spatial frequency analysis of rainfall intensity over the Ramon area. (a, b) Boxplots present the statistics of 10, 30, and 120 min for (a) 2-year and (b) 100-year intensities for the western (blue) and, eastern (red) part of the Ramon escarpment calculated using bootstrapping. The green dot presents the mean, the horizontal line presents the 50 quantile and the lower and upper box limits present the 25 and 75 quantiles, respectively. (c, d) 30-min rainfall intensities for 2- and 100-year return periods, respectively. Blue and red rectangles bound the pixels included in the analyses of the western and eastern sites, respectively. (e, f) 30-min rainfall intensity for 2-year and 100-year return periods (respectively) versus the mean annual rainfall (Figure 5) for pixels (denoted by gray plus signs in panels (c and d) along the Ramon escarpment northern rim. Note the similarity of the 2-year intensity along the escarpment and the significantly different intensity for the 100-year return period.

5.2. Implications for the Influence of Past Climates on Cliff Weathering, Slope Dissection, and the Formation of Talus-Flatirons

The present-day differences in climate, rainstorm characteristics, and erosion frequency along the Ramon escarpment correlate with the topographic differences and specifically with the increase in apparent fluvial activity, dissected slopes, and talus flatiron distribution in the NES. Cliff-slope evolution, and especially the generation of talus-flatiron sequences, was previously discussed in the context of Quaternary climate-cycles in arid areas. The climate has been hypothesized to influence the ratio between the outflux of transported debris along the slope versus the influx of debris from back-wearing of the cliff (e.g., Elorza & Martínez, 2001; Grossman & Gerson, 1987; Gutiérrez et al., 1998; Schmidt, 1996). Thus, potential temporal variations in the Negev climate, which, in turn, induce changes in the cliff weathering rate and erosion frequency during the Quaternary, could affect the topography of cliffs and sub-cliff slope along the Ramon escarpment.

Previous studies that dated talus flatirons in the eastern Negev argued that disconnected slopes were not formed during discrete phases of glacial-interglacial climatic cycles (Boroda et al., 2011, 2013). These authors stress the importance of hydroclimatic properties, flow frequency, and extreme events in modulating this landform, rather than general trends or cycles in mean climate. This notion is supported by evidence of permanent hyperaridity in these regions since the early Middle Pleistocene (Amit et al., 2006; Enzel et al., 2012). A rise in the frequency

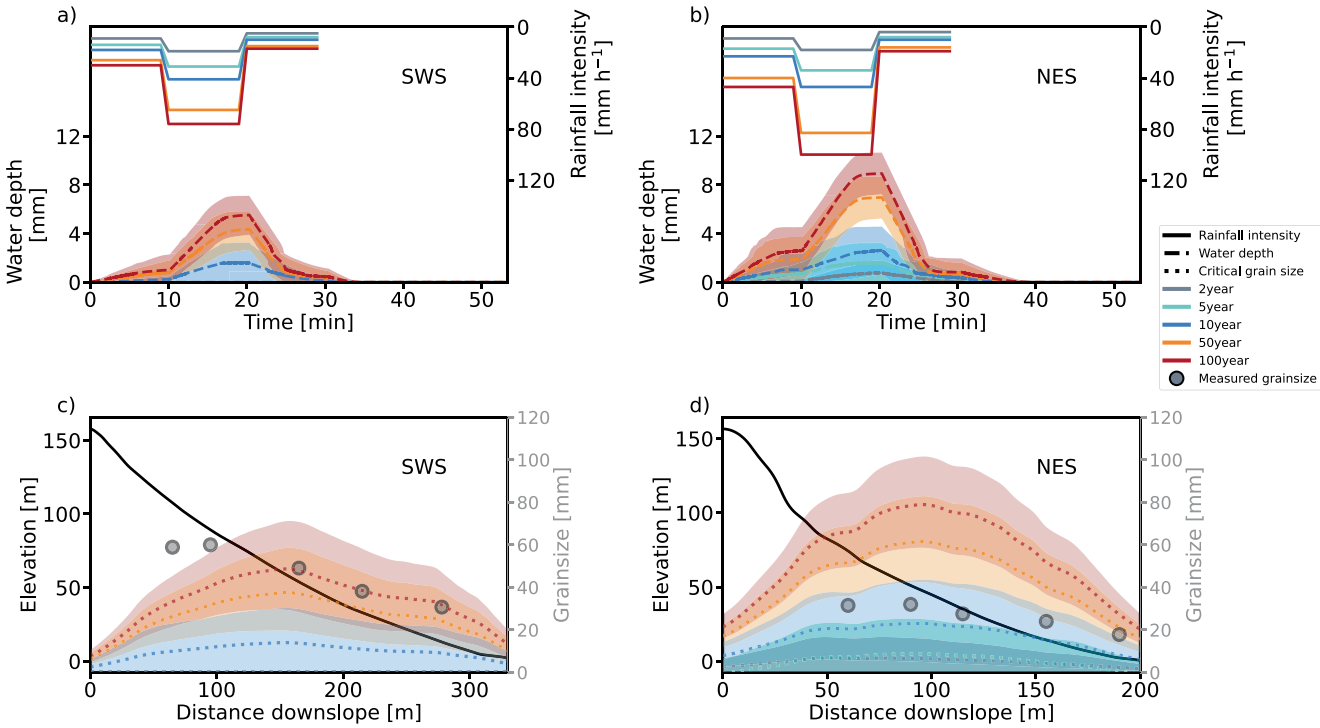

Figure 8. (a, b) An example of simulated water depth (bottom *y*-axis) during storms of different return periods (2-, 5-, 10-, 50-, and 100-year return periods, upper *y*-axis). The water depth is of a grid-node located 150 m from the cliff top along characteristic cliff-talus longitudinal slopes in the western and eastern sites (black lines in panels c and d, respectively). (c, d) Characteristic topographic profiles and maximal transportable grain size for storms of different return periods. The measured grain size (d_{50}, right *y*-axis, the same data that presented in Figure 5c) along the slope is shown as gray circles. Shaded areas denote the range of potential water depth (a, b) and maximal transportable grain size (c, d) incorporating uncertainties in Manning's n, the critical shear stress, and hydraulic conductivity. Colored curved are the median values of the uncertainty range.

of ARST-associated storms would result in rainstorms with higher intensity that could affect the evolution of the slopes. However, a higher ARST frequency would not necessarily result in an increase in the mean annual rainfall (e.g., Enzel et al., 2012), which is controlled primarily by the MC-associated precipitation events (e.g., Ahlborn et al., 2018). Also, according to present-day climatology, ARST-associated rainstorms contribute more rainfall to the northeastern part of Ramon escarpment than to the southwestern part (Marra et al., 2021a, 2021b). Therefore, the scenario of increased activity of ARST-associated storms would imply enhanced slope processes and fluvial activity in the northeastern part of the escarpment relative to the southwestern part.

Together with rainfall properties, temperature might have an important effect on the sediment budget along the cliffs due to frost action and freeze-thaw cycles by affecting the sediment production rate (e.g., Elorza & Martínez, 2001) and erosion frequency/magnitude (Sheehan & Ward, 2018; Ward et al., 2011). Under the current climate, cold days in the Negev are often associated with clear skies and low humidity. However, in the SWS, cold days sometimes occur when a high level of air moisture is observed (mainly during MC-associated events), which is rare in the eastern part of the escarpment. For example, the number of days with temperature below freezing measured at the Mitzpe Ramon station (located in between our west and east sites, Figure 1) is, on average, ∼1 day in 2 years (based on the minimum daily temperature, 1980–2021, https://ims.gov.il/en/ClimateAtlas). The ICON-IL temperature and humidity fields can be used to assess differences along the escarpment: the NES does not experience below-freezing days (a day with at least 1 hour below-freezing) with high humidity (hourly relative humidity over 90%), while the SWS experiences on average one such day every 2 years (Figure S6 in Supporting Information S1).

Frost action events were probably more frequent during the Last Glacial Maximum, considering a 6–8°C drop in the regional mean annual temperature (Keinan et al., 2019; Ludwig & Hochman, 2021; McGarry et al., 2004). Specifically, at the higher elevation site (SWS, ∼1,000 m), a relatively minor decrease in temperature could significantly increase the number of days with below freezing temperature. At the lower elevation northeastern

part (NES, ~600 m), however, this number would probably remain quite similar to the present conditions. For example, assuming no change in the variance of winter temperatures and humidity, with a 2°C decrease in the mean temperatures of the ICON-IL record, 2 days per year, on average, are predicted in the southwest, but only 1 day in 9 years is predicted for the northeast (Figure S6 in Supporting Information S1). A rising number of days with temperatures below freezing and high humidity in the southwest could lead to a higher rate of sediment deposition on the sub-cliff slopes in the SWS relative to the NES. An increase in days with high humidity and cold temperatures in the southwestern part of the escarpment is not necessarily compensated by the changes in rainfall extremes we discussed above, as the latter is associated mainly with ARST, which contributes mostly to the eastern part of the Negev. Considering a similar frequency of sediment mobilization (>100 years), an increase in the sediment influx from the cliff in the SWS will cover the sub-cliff slopes with sediment debris (Selby, 1982). The long and un-dissected slopes in the SWS may point to such a scenario. In addition, the present-day more effective extreme storms in the NES, as well as the potential for a higher frequency and magnitude of extreme storms under paleo-climatic conditions, can explain the shorter and dissected slopes in that area.

5.3. Rainstorm Characteristics Control Sediment Mobilization Beneath Cliffs

Slope hydrology simulated using synthetic storms based on modern rainstorm characteristics reveals that, along the NES, sediment mobilization occurs every >10–50 years (2%–10% yearly probability) (Figure 8d). In contrast, at the SWS, sediment is mobilized only under 50-100-year storms (1%–2%) (Figure 8c). It is possible that under past conditions, selective removal of the finer clasts during more frequent events occurred and led to coarsening of the materials on the slopes in a process called soil armoring (e.g., Cohen et al., 2009; Sharmeen & Willgoose, 2006). Under such a scenario the frequency of sediment mobilization of clasts in the SWS was probably still lower relative to the NES as the finer fractions of the clasts in the SWS are larger (i.e., d_{10}, Figure 5c). The low frequency of sediment mobilization by runoff in the SWS stems from the properties of the rainstorms (Figure 7), their hydrological interactions with the surface under the observed hydraulic conductivity (Table S1 in Supporting Information S1), and the relatively large size of clasts of their cliff-derived debris (Figure 5c). The persistence of the low erosion frequency in the SWS over Quaternary timescales might explain the observed longer and undissected slopes with greater debris cover (Selby, 1982). Accordingly, persistent of more frequent erosion during the Quaternary in the NES could explain the greater degree of channelization on the NES slopes (e.g., Sweeney et al., 2015) and higher exposed vertical cliffs (Figures 4 and 5).

Rainstorm impact on the Ramon escarpment warrants a comparison with other Negev sites. In the eastern Negev, numerous table-mountains (mesas) exist parallel to the western Dead Sea escarpment, which has been formed by significant down-cutting of streams draining into the Dead Sea basin (Haviv et al., 2010). These mesas are capped by resistant Campanian (Late Cretaceous) cherts that overlie softer Santonian chalk. Sub-cliff chalk slopes in the eastern Negev are sparsely vegetated (or practically barren) and heavily dissected by rills and gullies. This is similar to the eastern escarpment of the Ramon. The similarity between these two sites is attributed here to the geomorphic impact of extreme rainfall events, most probably born out in both areas from Active Red Sea Troughs. The mean annual rainfall in the eastern Negev and eastern Ramon escapement is quite low (<60 mm), and extreme rainstorms (return period >10 years) are associated with very high maximal intensities for short durations (>80 mm hr^{-1} for 10 minutes, Figure 7b, and Figure 6 in Shmilovitz et al., 2020). Similar to our results here, it has been shown that such extreme storms are the only effective storms in terms of runoff generation and mobilization of sediment on sub-cliff slopes in the eastern Negev (Shmilovitz et al., 2020). Having examined the eastern Negev chert table-mountains as well as the Ramon escarpment (central Negev), we conclude that extreme rainstorms have a significant influence on sediment mobilization and gully activity beneath cliffs.

In a manner similar to our conclusions from the Negev, rainstorm properties, event frequency-magnitude relationships, and erosion thresholds have long been hypothesized to have significant impacts on erosion and landscape evolution (Wolman & Gerson, 1978; Wolman & Miller, 1960). Previous results from numerical experiments have shown that, in the presence of erosion thresholds, rainstorm and discharge variability could influence erosion rates more than the mean condition (DiBiase & Whipple, 2011; Istanbulluoglu & Bras, 2006; Tucker, 2004). This is especially important for cases where most of the runoff events cannot erode the material on the bed (Tucker, 2004), such as coarse-grained sub-cliff slopes and gravel channels in drylands. In such cases, the interaction of rainstorm properties, hydrological forcings, and grain size could play a key role in setting erosion rates and the transition between colluvial and fluvial processes (Neely & DiBiase, 2023). This is demonstrated by the

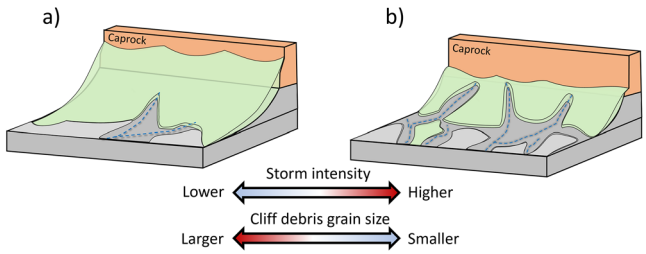

Figure 9. A conceptual model of the potential response of arid cliffs and sub-cliff slopes (talus slopes) to rainstorm regime and weathering pattern as reflected by cliff debris grain size. (a) Low-intensity rainstorm regimes and/or large cliff debris grains. The cliff-derived debris covers a large part of the caprock (above the lithological contact) and the debris layer is thick. The sub-cliff slope is long with a concave longitudinal profile. The sub-cliff slope is slightly incised in the lower parts. (b) Cliff-slope morphology under a high-intensity rainstorm regime and/or small cliff debris grains. The debris cover is thin, and the slopes are linear, short, and highly dissected. Intense gully activity led to cliff-detached talus slopes (talus flatiron).

increase in sub-cliff channel density and decrease in slope length toward the northeastern side of the Ramon escarpment (Figures 3–5).

5.4. Insight Into Climatic Impacts on Cliff-Slope Morphology Along Escarpments in Drylands Beyond the Negev

Many previous studies have focused on quantifying the effect of spatial variations in climatic properties on topography and erosion rates over large spatial scales, such as in mountain ranges (e.g., Adams et al., 2020; Leonard & Whipple, 2021), where variations in daily rainfall/discharge can be pronounced. Less attention has been paid to hillslopes located in dry regions, where finer changes in spatiotemporal processes could cause significant changes in the magnitude of surface processes. For soil-covered hillslopes, bedrock weathering rates increase with the transition from arid and hyperarid regions (mean annual rainfall >100 mm) to semi-arid zones where the importance of chemical and biotic-driven weathering increases relative to slow salt weathering (Owen et al., 2011). Toward the sub-humid regions (>700 mm), the increase in annual rainfall also drives changes in overland flow patterns and sediment transport mechanisms, including increased bioturbation and throughflow, thereby affecting hillslope length, gradient and catchment dissection (Chadwick et al., 2013). Schmidt (2009) presented a compilation of morpho-types for layered, cliff-associated rocky hillslopes as a function of annual rainfall (ranging between ∼150 and ∼600 mm year^{-1}; beyond the mean annual rainfall over the Ramon escarpment) and altitude. Based on his data, with increasing annual rainfall, the sub-cliff slopes are less dissected and are longer relative to sub-cliff slopes in drier areas, highlighting the role of vegetation cover. While these studies highlight the mean climate as a potential trigger for changes in hillslope surface processes, in our sites, the differences in annual rainfall are small and cannot account for the observed topographic difference. We demonstrate how significant changes in cliff-slope form in a hyperarid setting (<100 mm) can be explained by the spatial variation in the sub-hourly rainfall intensity of extreme events.

Based on our results, we suggest a conceptual model for the evolution of cliff and sub-cliff slopes along arid escarpments (Figure 9), where areas with higher storm intensity, and/or smaller cliff-derived grain size, are characterized by less extensive debris cover, more dissected sub-cliff slopes and, preserved vertical cliffs. These morphologic transitions could occur opposite to the general trend in annual precipitation. As drylands are well known to be associated with higher rainfall and runoff variability (Molnar et al., 2006; Morin, 2011; Rossi et al., 2016; Schick, 1988; Yair & Lavee, 1985), and statistically tend to experience higher extreme rainstorm events (Marra et al., 2017; Marra & Morin, 2015), this conceptual model emphasizes the possibility that the morphology of other dryland escarpments, such as in southern Morocco (Littmann & Schmidt, 1989), the Book Cliffs in the Colorado Plateau (McCarroll et al., 2021) and cliffs along the great Victoria desert in southern Australia (Ollier & Tuddenham, 1962), record climatic signals on a similar fine-scale resolution. Additional worldwide field observations could provide analogs for the potential impacts of temporal climatic changes. These effects include cliff-slope morphology, cliff retreat rate, and talus-flatiron formation.

6. Conclusions

We examined the sensitivity of a 40 km long hyperarid escarpment to storm-scale forcing at the sub-regional scale using a combination of methods including topographic analysis of escarpment morphology, storm-scale statistical analysis, and hydrological simulations of synthetic storms. A pronounced gradient in the mean annual rainfall exists along the escarpment controlled by the orographic effect. Storm-scale statistical analysis reveals that extreme, short-duration, high intensity storms (return periods >10 years) increase toward the drier part of the escarpment. Based on hydrological simulations, sediment is mobilized every 10–50 years on the eastern drier sub-cliff slopes under the present climate. However, at the western wetter part of the escarpment, clasts are transported only under >50-year storms. Exposed cliff bedrock patches, shorter sub-cliff slopes, and increased gullying activity on the drier side are all possible consequences of the higher frequency of sediment mobilization. Our findings indicate that in this arid environment, escarpment topography correlates better with short duration (sub-hourly) extreme rainstorms than with mean annual precipitation. This can be explained by the high impact

of discrete and rare rainstorms on runoff generation and sediment mobilization. We conclude that within the present hyperarid conditions, significant variations in rainstorm properties exist along a relatively short distance (<40 km), and these rainstorm properties leave a significant imprint on escarpment morphology. We propose that the evolution of dryland escarpments worldwide may be affected by small-scale climatic variations, especially those associated with rainstorms. Illuminating these links are needed to better understand landscape evolution in dry regions under Quaternary climate change.

Data Availability Statement

We used the open-source TopoToolBox MATLAB software for topographic analysis. All functions used for the hydrological simulations are based on the open-source Landlab modeling library and the code used in this study for hydrological simulations is available in an online repository: yuvalsmilo (2023), https://doi.org/10.5281/zenodo.8161362. Rain gauges data were provided by the Israel Meteorological Service (https://ims.gov.il/en) and the Arava Drainage Authority. Ramon stream discharges were provided by the Israel Hydrological Service.

Acknowledgments
This study was partially funded by the U.S.-Israel Binational Science Foundation (2020664 to Yehouda Enzel and Efrat Morin), the U.S. National Science Foundation (2100753, 2100702, 2104102, 2148762), the BARD project (IS-5124-18 to Efrat Morin), and a fellowship to YS from the Hebrew University Advanced School for Environmental Studies and the Keren Kayemeth LeIsrael-Jewish National Fund. MA was supported by an ETH Zurich postdoctoral fellowship (21-1 FEL-67) and by the Stiftung fur naturwissenschaftliche und technische Forshung as well as the ETH Zurich Foundation. The authors thank Barak Izrael and Niv Keren for field work assistance.

References

Adams, B. A., Whipple, K. X., Forte, A. M., Heimsath, A. M., & Hodges, K. V. (2020). Climate controls on erosion in tectonically active landscapes. *Science Advances*, *6*(42). https://doi.org/10.1126/sciadv.aaz3166

Ahlborn, M., Armon, M., Ben Dor, Y., Neugebauer, I., Schwab, M. J., Tjallingii, R., et al. (2018). Increased frequency of torrential rainstorms during a regional late Holocene eastern Mediterranean drought. *Quaternary Research*, *89*(2), 425–431. https://doi.org/10.1017/qua.2018.9

Allamano, P., Claps, P., Laio, F., & Thea, C. (2009). A data-based assessment of the dependence of short-duration precipitation on elevation. *Physics and Chemistry of the Earth*, Parts A/B/C, *34*(10–12), 635–641. https://doi.org/10.1016/J.PCE.2009.01.001

Alpert, P., Neeman, B. U., & Shay-El, Y. (2016). Climatological analysis of Mediterranean cyclones using ECMWF data (Vol. *42*, pp. 65–77). https://doi.org/10.3402/TELLUSA.V42I1.11860

Amit, R., Enzel, Y., & Sharon, D. (2006). Permanent Quaternary hyperaridity in the Negev, Israel, resulting from regional tectonics blocking Mediterranean frontal systems. *Geology*, *34*(6), 509–512. https://doi.org/10.1130/G22354.1

Amit, R., & Gerson, R. (1986). The evolution of Holocene Reg (gravelly) soils in deserts. An example from the Dead Sea region. *Catena*, *13*(1–2), 59–79. https://doi.org/10.1016/S0341-8162(86)80005-4

Armon, M., Dente, E., Smith, J. A., Enzel, Y., & Morin, E. (2018). Synoptic-scale control over modern rainfall and flood patterns in the Levant drylands with implications for past climates. *Journal of Hydrometeorology*, *19*(6), 1077–1096. https://doi.org/10.1175/JHM-D-18-0013.1

Armon, M., Marra, F., Enzel, Y., Rostkier-Edelstein, D., Garfinkel, C. I., Adam, O., et al. (2022). Reduced rainfall in future heavy precipitation events related to contracted rain area despite increased rain rate. *Earth's Future*, *10*(1), e2021EF002397. https://doi.org/10.1029/2021ef002397

Armon, M., Marra, F., Enzel, Y., Rostkier-Edelstein, D., & Morin, E. (2020). Radar-based characterisation of heavy precipitation in the eastern Mediterranean and its representation in a convection-permitting model. *Hydrology and Earth System Sciences*, *24*(3), 1227–1249. https://doi.org/10.5194/hess-24-1227-2020

Armon, M., Morin, E., & Enzel, Y. (2019). Overview of modern atmospheric patterns controlling rainfall and floods into the Dead Sea: Implications for the lake's sedimentology and paleohydrology. *Quaternary Science Reviews*, *216*, 58–73. https://doi.org/10.1016/J.QUASCIREV.2019.06.005

Ashbel, D. (1938). Great floods in Sinai Peninsula, Palestine, Syria and the Syrian Desert, and the influence of the red sea on their formation. *Quarterly Journal of the Royal Meteorological Society*, *64*(277), 635–639. https://doi.org/10.1002/qj.49706427716

Avanzi, F., De Michele, C., Gabriele, S., Ghezzi, A., & Rosso, R. (2015). Orographic signature on extreme precipitation of short durations. *Journal of Hydrometeorology*, *16*(1), 278–294. https://doi.org/10.1175/JHM-D-14-0063.1

Avni, Y. (1991). The geology, paleogeography and landscape evolution in the central Negev highlands and the western Ramon structure. *The Geological Survey*Rep GSI/6/91 (in Hebrew, English abstract).

Ban, N., Schmidli, J., & Schär, C. (2014). Evaluation of the convection-resolving regional climate modeling approach in decade-long simulations. *Journal of Geophysical Research*, *119*(13), 7889–7907. https://doi.org/10.1002/2014JD021478

Barnhart, K. R., Hutton, E. W. H., Tucker, G. E., Gasparini, N. M., Istanbulluoglu, E., Hobley, D. E. J., et al. (2020). Short communication: Landlab v2.0: A software package for Earth surface dynamics. *Earth Surface Dynamics Discussions*, 1–25. https://doi.org/10.5194/esurf-2020-12

Belachsen, I., Marra, F., Peleg, N., & Morin, E. (2017). Convective rainfall in a dry climate: Relations with synoptic systems and flash-flood generation in the Dead Sea region. *Hydrology and Earth System Sciences*, *21*(10), 5165–5180. https://doi.org/10.5194/hess-21-5165-2017

Bentor, Y. K., & Vroman, A. (1952). *A new occurrence of the Marine Triassic in Israel* (Vol. 1, pp. 1–98). Research Council of Israel Bulletin, Section G, Geo-sciences, G.

Bookhagen, B., & Strecker, M. R. (2012). Spatiotemporal trends in erosion rates across a pronounced rainfall gradient: Examples from the southern Central Andes. *Earth and Planetary Science Letters*, *327–328*, 97–110. https://doi.org/10.1016/j.epsl.2012.02.005

Boroda, R., Amit, R., Matmon, A., ASTER Team, Finkel, R., Porat, N., et al. (2011). Quaternary-scale evolution of sequences of talus flatirons in the hyperarid Negev. *Geomorphology*, *127*(1–2), 41–52. https://doi.org/10.1016/j.geomorph.2010.12.003

Boroda, R., Matmon, A., Amit, R., Haviv, I., Porat, N., Rood, D., et al. (2013). Long-term talus flatirons formation in the hyperarid northeastern Negev, Israel. *Quaternary Research*, *79*(2), 256–267. https://doi.org/10.1016/j.yqres.2012.11.012

Bruthans, J., Filippi, M., Schweigstillová, J., & Řihošek, J. (2017). Quantitative study of a rapidly weathering overhang developed in an artificially wetted sandstone cliff. *Earth Surface Processes and Landforms*, *42*(5), 711–723. https://doi.org/10.1002/esp.4016

Buffington, J. M., & Montgomery, D. R. (1997). A systematic analysis of eight decades of incipient motion studies, with special reference to gravel-bedded rivers. *Water Resources Research*, *33*(8), 1993–2029. https://doi.org/10.1029/96WR03190

Chadwick, O. A., Roering, J. J., Heimsath, A. M., Levick, S. R., Asner, G. P., & Khomo, L. (2013). Shaping post-orogenic landscapes by climate and chemical weathering. *Geology*, *41*(11), 1171–1174. https://doi.org/10.1130/G34721.1

Chow, V. T., Maidment, D. R., & Mays, L. W. (1988). In C. B. J. & M. John (Eds.), *Applied hydrology*. McGraw-Hill.

Cohen, S., Willgoose, G., & Hancock, G. (2009). The mARM spatially distributed soil evolution model: A computationally efficient modeling framework and analysis of hillslope soil surface organization. *Journal of Geophysical Research*, *114*(3), F03001. https://doi.org/10.1029/2008JF001214

Dayan, U., Lensky, I. M., Ziv, B., & Khain, P. (2021). Atmospheric conditions leading to an exceptional fatal flash flood in the Negev Desert, Israel. *Natural Hazards and Earth System Sciences*, *21*(5), 1583–1597. https://doi.org/10.5194/nhess-21-1583-2021

Dayan, U., & Morin, E. (2006). Flash flood–producing rainstorms over the Dead Sea: A review.

de Almeida, G. A. M., Bates, P., Freer, J. E., & Souvignet, M. (2012). Improving the stability of a simple formulation of the shallow water equations for 2-D flood modeling. *Water Resources Research*, *48*(5). https://doi.org/10.1029/2011WR011570

de Vries, A. J., Tyrlis, E., Edry, D., Krichak, S. O., Steil, B., & Lelieveld, J. (2013). Extreme precipitation events in the Middle East: Dynamics of the active Red Sea trough. *Journal of Geophysical Research: Atmospheres*, *118*(13), 7087–7108. https://doi.org/10.1002/jgrd.50569

DiBiase, R. A., & Whipple, K. X. (2011). The influence of erosion thresholds and runoff variability on the relationships among topography, climate, and erosion rate. *Journal of Geophysical Research*, *116*(4), 1–17. https://doi.org/10.1029/2011JF002095

Dunkerley, D. (2012). Effects of rainfall intensity fluctuations on infiltration and runoff: Rainfall simulation on dryland soils, Fowlers Gap, Australia. *Hydrological Processes*, *26*(15), 2211–2224. https://doi.org/10.1002/hyp.8317

Dunkerley, D. (2019). Rainfall intensity bursts and the erosion of soils: An analysis highlighting the need for high temporal resolution rainfall data for research under current and future climates. *Earth Surface Dynamics*, *7*(2), 345–360. https://doi.org/10.5194/esurf-7-345-2019

Elorza, M. G., & Martínez, V. S. (2001). Multiple talus flatirons, variations of scarp retreat rates and the evolution of slopes in Almazán Basin (semi-arid central Spain). *Geomorphology*, *38*(1–2), 19–29.

El-Samra, R., Bou-Zeid, E., Bangalath, H. K., Stenchikov, G., & El-Fadel, M. (2017). Future intensification of hydro-meteorological extremes: Downscaling using the weather research and forecasting model. *Climate Dynamics*, *49*(11–12), 3765–3785. https://doi.org/10.1007/s00382-017-3542-z

Ely, L. L., Enzel, Y., Baker, V. R., & Cayan, D. R. (1993). A 5000-year record of extreme floods and climate change in the southwestern United States. *Science*, *262*(5132), 410–412. https://doi.org/10.1126/science.262.5132.410

Enzel, Y., Amit, R., Dayan, U., Crouvi, O., Kahana, R., Ziv, B., & Sharon, D. (2008). The climatic and physiographic controls of the eastern Mediterranean over the late Pleistocene climates in the southern Levant and its neighboring deserts. *Global and Planetary Change*, *60*(3–4), 165–192. https://doi.org/10.1016/J.GLOPLACHA.2007.02.003

Enzel, Y., Amit, R., Grodek, T., Ayalon, A., Lekach, J., Porat, N., et al. (2012). Late Quaternary weathering, erosion, and deposition in Nahal Yael, Israel: An "impact of climatic change on an arid watershed". *Bulletin of the Geological Society of America*, *124*(5–6), 705–722. https://doi.org/10.1130/B30538.1

Ferrier, K. L., Huppert, K. L., & Perron, J. T. (2013). Climatic control of bedrock river incision. *Nature*, *496*(7444), 206–209. https://doi.org/10.1038/nature11982

Fisher, R. A., & Tippett, L. H. C. (1928). Limiting forms of the frequency distribution of the largest or smallest member of a sample. In *Mathematical proceedings of the Cambridge philosophical society* (Vol. 24, pp. 180–190). Cambridge University Press.

Formetta, G., Marra, F., Dallan, E., Zaramella, M., & Borga, M. (2022). Differential orographic impact on sub-hourly, hourly, and daily extreme precipitation. *Advances in Water Resources*, *159*, 104085. https://doi.org/10.1016/J.ADVWATRES.2021.104085

Garfunkel, Z. (1964). Tectonic phenomena along the Ramon lineament. *Israel Journal of Earth Sciences*, *13*, 186.

Garrels, R. M., & Lasaga, A. C. (1983). The carbonate-silicate geochemical cycle and its effect on atmospheric carbon dioxide over the past 100 million years. *American Journal of Science*, *283*(7), 641–683. https://doi.org/10.2475/ajs.283.7.641

Gerson, R. (1982). Talus relicts in deserts: A key to major climatic fluctuations. *Israel Journal of Earth-Sciences*, *31*, 123–132.

Goldreich, Y. (1994). The spatial distribution of annual rainfall in Israel—A review. *Theoretical and Applied Climatology*, *50*(1), 45–59. https://doi.org/10.1007/bf00864902

Goldreich, Y. (2003). The climate of Israel. *The Climate of Israel*. https://doi.org/10.1007/978-1-4615-0697-3

Goodrich, D. C., Faurès, J.-M., Woolhiser, D. A., Lane, L. J., & Sorooshian, S. (1995). Measurement and analysis of small-scale convective storm rainfall variability. *Journal of Hydrology*, *173*(1–4), 283–308. https://doi.org/10.1016/0022-1694(95)02703-R

Goudenhoofdt, E., Delobbe, L., & Willems, P. (2017). Regional frequency analysis of extreme rainfall in Belgium based on radar estimates. *Hydrology and Earth System Sciences*, *21*(10), 5385–5399. https://doi.org/10.5194/hess-21-5385-2017

Goudie, A. S., Viles, H. A., & Parker, A. G. (1997). Monitoring of rapid salt weathering in the central Namib Desert using limestone blocks. Retrieved from https://ac.els-cdn.com/S0140196397902974/1-s2.0-S0140196397902974-main.pdf?_tid=8a988b3f-2335-4c49-96df-3aa8f989561d&acdnat=1551862787_39ed782d6a7daa1da75a36c6696992a0

Grossman, S., & Gerson, R. (1987). Fluviatile deposits and morphology of alluvial surfaces as indicators of Quaternary environmental changes in the southern Negev, Israel. *Geological Society, London, Special Publications*, *35*(1), 17–29. https://doi.org/10.1144/gsl.sp.1987.035.01.03

Gustafsson, N., Janjić, T., Schraff, C., Leuenberger, D., Weissmann, M., Reich, H., et al. (2018). Survey of data assimilation methods for convective-scale numerical weather prediction at operational centres. *Quarterly Journal of the Royal Meteorological Society*, *144*(713), 1218–1256. https://doi.org/10.1002/QJ.3179

Gutiérrez, M., Sancho, C., & Arauzo, T. (1998). Scarp retreat rates in semiarid environments from talus flatirons (Ebro Basin, NE Spain). *Geomorphology*, *25*(1–2), 111–121. https://doi.org/10.1016/s0169-555x(98)00034-8

Haviv, I., Enzel, Y., Whipple, K. X., Zilberman, E., Matmon, A., Stone, J., & Fifield, K. L. (2010). Evolution of vertical knickpoints (waterfalls) with resistant caprock: Insights from numerical modeling. *Journal of Geophysical Research*, *115*(F3), F03028. https://doi.org/10.1029/2008jf001187

Herman, F., Seward, D., Valla, P. G., Carter, A., Kohn, B., Willett, S. D., & Ehlers, T. A. (2013). Worldwide acceleration of mountain erosion under a cooling climate. *Nature*, *504*(7480), 423–426. https://doi.org/10.1038/nature12877

Hobley, D. E. J., Adams, J. M., Siddhartha Nudurupati, S., Hutton, E. W. H., Gasparini, N. M., Istanbulluoglu, E., & Tucker, G. E. (2017). Creative computing with Landlab: An open-source toolkit for building, coupling, and exploring two-dimensional numerical models of Earth-surface dynamics. *Earth Surface Dynamics*, *5*(1), 21–46. https://doi.org/10.5194/esurf-5-21-2017

Istanbulluoglu, E., & Bras, R. L. (2006). On the dynamics of soil moisture, vegetation, and erosion: Implications of climate variability and change. *Water Resources Research*, *42*(6). https://doi.org/10.1029/2005WR004113

Kahana, R., Ziv, B., Enzel, Y., & Dayan, U. (2002). Synoptic climatology of major floods in the Negev Desert, Israel. *International Journal of Climatology*, *22*(7), 867–882. https://doi.org/10.1002/joc.766

Keinan, J., Bar-Matthews, M., Ayalon, A., Zilberman, T., Agnon, A., & Frumkin, A. (2019). Paleoclimatology of the Levant from Zalmon Cave speleothems, the northern Jordan valley, Israel. *Quaternary Science Reviews*, *220*, 142–153. https://doi.org/10.1016/j.quascirev.2019.07.018

Khain, P., Levi, Y., Shtivelman, A., Vadislavsky, E., Brainin, E., & Stav, N. (2020). Improving the precipitation forecast over the Eastern Mediterranean using a smoothed time-lagged ensemble. *Meteorological Applications*, *27*(1). https://doi.org/10.1002/met.1840

Kidwell, M. R., Weltz, M. A., & Phillip Guertin, D. (1997). Estimation of Green-Ampt effective hydraulic conductivity for rangelands. *Journal of Range Management*, *50*(3), 290–299. https://doi.org/10.2307/4003732
Krenkel, E. (1924). Der Syrische Bogen: Centralblatt fur Mineralogie, Geologie und Paleontologie: Jahrgana (pp. 274–313).
Kunz, M., Blahak, U., Handwerker, J., Schmidberger, M., Punge, H. J., Mohr, S., et al. (2018). The severe hailstorm in southwest Germany on 28 July 2013: Characteristics, impacts and meteorological conditions. *Quarterly Journal of the Royal Meteorological Society*, *144*(710), 231–250. https://doi.org/10.1002/QJ.3197
Lamp, J. L., Marchant, D. R., Mackay, S. L., & Head, J. W. (2017). Thermal stress weathering and the spalling of Antarctic rocks. *Journal of Geophysical Research: Earth Surface*, *122*(1), 3–24. https://doi.org/10.1002/2016JF003992
Langbein, W. B., & Schumm, S. A. (1958). Yield of sediment in relation to mean annual precipitation. *Eos, Transactions American Geophysical Union*, *39*(6), 1076–1084. https://doi.org/10.1029/TR039i006p01076
Leonard, J. S., & Whipple, K. X. (2021). Influence of spatial rainfall gradients on river longitudinal profiles and the topographic expression of spatially and temporally variable climates in mountain landscapes. *Journal of Geophysical Research: Earth Surface*, *126*(12), e2021JF006183. https://doi.org/10.1029/2021JF006183
Littmann, T., & Schmidt, K. H. (1989). The response of different relief units to climatic change in an arid environment (southern Morocco). *Catena*, *16*(4–5), 343–355. https://doi.org/10.1016/0341-8162(89)90019-2
Liu, C., Ikeda, K., Rasmussen, R., Barlage, M., Newman, A. J., Prein, A. F., et al. (2017). Continental-scale convection-permitting modeling of the current and future climate of North America. *Climate Dynamics*, *49*(1–2), 71–95. https://doi.org/10.1007/s00382-016-3327-9
Liu, H., Koren, I., Altaratz, O., Heiblum, R. H., Khain, P., Ouyang, X., & Guo, J. (2021). Oscillations in deep-open-cells during winter Mediterranean cyclones. *Npj Climate and Atmospheric Science*, *4*(1), 1–7. https://doi.org/10.1038/s41612-021-00168-9
Ludwig, P., & Hochman, A. (2021). Last glacial maximum hydro-climate and cyclone characteristics in the Levant: A regional modelling perspective. *Environmental Research Letters*, *17*(1), 014053. https://doi.org/10.1088/1748-9326/ac46ea
Marra, F., Armon, M., Adam, O., Zoccatelli, D., Gazal, O., Garfinkel, C. I., et al. (2021a). Toward narrowing uncertainty in future projections of local extreme precipitation. *Geophysical Research Letters*, *48*(5). https://doi.org/10.1029/2020GL091823
Marra, F., Armon, M., Borga, M., & Morin, E. (2021b). Orographic effect on extreme precipitation statistics peaks at hourly time scales. *Geophysical Research Letters*, *48*(5), e2020GL091498. https://doi.org/10.1029/2020GL091498
Marra, F., Borga, M., & Morin, E. (2020). A unified framework for extreme subdaily precipitation frequency analyses based on ordinary events. *Geophysical Research Letters*, *47*(18), 1–8. https://doi.org/10.1029/2020GL090209
Marra, F., & Morin, E. (2015). Use of radar QPE for the derivation of Intensity-Duration-Frequency curves in a range of climatic regimes. *Journal of Hydrology*, *531*, 427–440. https://doi.org/10.1016/j.jhydrol.2015.08.064
Marra, F., & Morin, E. (2018). Autocorrelation structure of convective rainfall in semiarid-arid climate derived from high-resolution X-Band radar estimates. *Atmospheric Research*, *200*, 126–138. https://doi.org/10.1016/j.atmosres.2017.09.020
Marra, F., Morin, E., Peleg, N., Mei, Y., & Anagnostou, E. N. (2017). Intensity-duration-frequency curves from remote sensing rainfall estimates: Comparing satellite and weather radar over the eastern Mediterranean. *Hydrology and Earth System Sciences*, *21*(5), 2389–2404. https://doi.org/10.5194/hess-21-2389-2017
Marra, F., Zoccatelli, D., Armon, M., & Morin, E. (2019). A simplified MEV formulation to model extremes emerging from multiple nonstationary underlying processes. *Advances in Water Resources*, *127*, 280–290. https://doi.org/10.1016/j.advwatres.2019.04.002
McCarroll, N. R., Pederson, J. L., Hidy, A. J., & Rittenour, T. M. (2021). Chronostratigraphy of talus flatirons and piedmont alluvium along the book Cliffs, Utah—Testing models of dryland escarpment evolution. *Quaternary Science Reviews*, *274*, 107286. https://doi.org/10.1016/j.quascirev.2021.107286
McGarry, S., Bar-Matthews, M., Matthews, A., Vaks, A., Schilman, B., & Ayalon, A. (2004). Constraints on hydrological and paleotemperature variations in the Eastern Mediterranean region in the last 140 ka given by the δD values of speleothem fluid inclusions. *Quaternary Science Reviews*, *23*(7–8), 919–934. https://doi.org/10.1016/j.quascirev.2003.06.020
Michaelides, K., & Martin, G. J. (2012). Sediment transport by runoff on debris-mantled dryland hillslopes. *Journal of Geophysical Research*, *117*(F3), F03014. https://doi.org/10.1029/2012JF002415
Miller, D. M., Schmidt, K. M., Mahan, S. A., McGeehin, J. P., Owen, L. A., Barron, J. A., et al. (2010). Holocene landscape response to seasonality of storms in the Mojave Desert. *Quaternary International*, *215*(1–2), 45–61. https://doi.org/10.1016/j.quaint.2009.10.001
Minder, J. R., Letcher, T. W., Campbell, L. S., Veals, P. G., & Steenburgh, W. J. (2015). The evolution of lake-effect convection during landfall and orographic uplift as observed by profiling radars. *Monthly Weather Review*, *143*(11), 4422–4442. https://doi.org/10.1175/MWR-D-15-0117.1
Molnar, P., Anderson, R. S., Kier, G., & Rose, J. (2006). Relationships among probability distributions of stream discharges in floods, climate, bed load transport, and river incision. *Journal of Geophysical Research*, *111*(F2), F02001. https://doi.org/10.1029/2005JF000310
Molnar, P., & England, P. (1990). Late Cenozoic uplift of mountain ranges and global climate change: Chicken or egg? *Nature*, *346*(6279), 29–34. https://doi.org/10.1038/346029a0
Morin, E. (2011). To know what we cannot know: Global mapping of minimal detectable absolute trends in annual precipitation. *Water Resources Research*, *47*(7), 7505. https://doi.org/10.1029/2010WR009798
Morin, E., & Gabella, M. (2007). Radar-based quantitative precipitation estimation over Mediterranean and dry climate regimes. *Journal of Geophysical Research*, *112*(20), 1–13. https://doi.org/10.1029/2006JD008206
Morin, E., Marra, F., & Armon, M. (2020). Dryland precipitation climatology from satellite observations. In *Satellite precipitation measurement* (pp. 843–859). Springer.
Nativ, R., & Mazor, E. (1987). Rain events in an arid environment—Their distribution and ionic and isotopoic composition patterns: Makhtesh Ramon basin, Israel. *Journal of Hydrology*, *89*(3–4), 205–237. https://doi.org/10.1016/0022-1694(87)90180-6
Neely, A. B., & DiBiase, R. A. (2020). Drainage area, bedrock fracture spacing, and weathering controls on landscape-scale patterns in surface sediment grain size. *Journal of Geophysical Research: Earth Surface*, *125*(10), e2020JF005560. https://doi.org/10.1029/2020JF005560
Neely, A. B., & DiBiase, R. A. (2023). Sediment controls on the transition from debris flow to fluvial channels in steep mountain ranges. *Earth Surface Processes and Landforms*, *48*(7), 1342–1361. https://doi.org/10.1002/esp.5553
Nicholson, S. E. (2011). Dryland climatology. *Dryland Climatology*. https://doi.org/10.1017/CBO9780511973840
Olen, S. M., Bookhagen, B., Hoffmann, B., Sachse, D., Adhikari, D. P., & Strecker, M. R. (2015). Understanding erosion rates in the Himalayan orogen: A case study from the Arun valley. *Journal of Geophysical Research: Earth Surface*, *120*(10), 2080–2102. https://doi.org/10.1002/2014JF003410
Ollier, C. D., & Tuddenham, W. G. (1962). Slope development at Coober Pedy, South Australia. *Journal of the Geological Society of Australia*, *9*(1), 91–105. https://doi.org/10.1080/00167616208728518
Owen, J. J., Amundson, R., Dietrich, W. E., Nishiizumi, K., Sutter, B., & Chong, G. (2011). The sensitivity of hillslope bedrock erosion to precipitation. *Earth Surface Processes and Landforms*, *36*(1), 117–135. https://doi.org/10.1002/esp.2083

Parsons, A. J., Abrahams, A. D., & Howard, A. D. (2009). Rock-mantled slopes. In A. J. Parsons & A. D. Abrahams (Eds.), *Gemorphology of desert environments* (2nd ed.). Springer US.

Pawlik, Ł. (2013). The role of trees in the geomorphic system of forested hillslopes—A review. *Earth-Science Reviews*, *126*, 250–265. https://doi.org/10.1016/j.earscirev.2013.08.007

Peizhen, Z., Molnar, P., & Downs, W. R. (2001). Increased sedimentation rates and grain sizes 2–4 Myr ago due to the influence of climate change on erosion rates. *Nature*, *410*(6831), 891–897. https://doi.org/10.1038/35073504

Perron, J. T. (2017). Climate and the pace of erosional landscape evolution. *Annual Review of Earth and Planetary Sciences*, *45*(1), 561–591. annurev-earth-060614-105405. https://doi.org/10.1146/annurev-earth-060614-105405

QGIS. (2019). *QGIS geographic information system*. QGIS Association.

Rinat, Y., Marra, F., Armon, M., Metzger, A., Levi, Y., Khain, P., et al. (2021). Hydrometeorological analysis and forecasting of a 3 d flash-flood-triggering desert rainstorm. *Natural Hazards and Earth System Sciences*, *21*(3), 917–939. https://doi.org/10.5194/nhess-21-917-2021

Rinat, Y., Marra, F., Zoccatelli, D., & Morin, E. (2018). Controls of flash flood peak discharge in Mediterranean basins and the special role of runoff-contributing areas. *Journal of Hydrology*, *565*(August), 846–860. https://doi.org/10.1016/j.jhydrol.2018.08.055

Roberts, N. (2008). Assessing the spatial and temporal variation in the skill of precipitation forecasts from an NWP model. *Meteorological Applications*, *15*(1), 163–169. https://doi.org/10.1002/MET.57

Roe, G. H. (2004). Orographic precipitation (Vol. *33*, pp. 645–671). https://doi.org/10.1146/ANNUREV.EARTH.33.092203.122541

Romem, M., Ziv, B., & Saaroni, H. (2007). Scenarios in the development of Mediterranean cyclones. *Advances in Geosciences*, *12*, 59–65. https://doi.org/10.5194/adgeo-12-59-2007

Rossi, M. W., Whipple, K. X., & Vivoni, E. R. (2016). Precipitation and evapotranspiration controls on daily runoff variability in the contiguous United States and Puerto Rico. *Journal of Geophysical Research: Earth Surface*, *121*(1), 128–145. https://doi.org/10.1002/2015JF003446

Rostkier-Edelstein, D., Liu, Y., Wu, W., Kunin, P., Givati, A., & Ge, M. (2014). Towards a high-resolution climatography of seasonal precipitation over Israel. *International Journal of Climatology*, *34*(6), 1964–1979. https://doi.org/10.1002/JOC.3814

Rubin, S., Ziv, B., & Paldor, N. (2007). Tropical plumes over eastern North Africa as a source of rain in the Middle East. *Monthly Weather Review*, *135*(12), 4135–4148. https://doi.org/10.1175/2007MWR1919.1

Sadeh, Y., Cohen, H., Maman, S., Blumberg, D., Sadeh, Y., Cohen, H., et al. (2018). Evaluation of Manning's n roughness coefficient in arid environments by using SAR backscatter. *Remote Sensing*, *10*(10), 1505. https://doi.org/10.3390/rs10101505

Schär, C., Ban, N., Fischer, E. M., Rajczak, J., Schmidli, J., Frei, C., et al. (2016). Percentile indices for assessing changes in heavy precipitation events. *Climatic Change*, *137*(1–2), 201–216. https://doi.org/10.1007/S10584-016-1669-2/FIGURES/4

Schick, A. P. (1988). Hydrologic aspects of floods in extreme arid environments. In *Flood geomorphology* (pp. 189–203). John Wiley & Sons. 14 Fig, 2 Tab, 39 Ref.

Schmidt, K. H. (1996). Talus and pediment flatirons, indicators of climatic change on scarp slopes on the Colorado Plateau, USA. *Zeitschrift für Geomorphologie - Supplementbände*(103), 135–158.

Schmidt, K.-H. (2009). Hillslopes as evidence of climatic change. In *Geomorphology of desert environments* (pp. 675–694). Springer.

Schumm, S. A., & Chorley, R. J. (1966). *Talus weathering and scarp recession in the Colorado Plateaus*. US Geological Survey.

Schwanghart, W., & Scherler, D. (2014). Short communication: TopoToolbox 2-MATLAB-based software for topographic analysis and modeling in Earth surface sciences. *Earth Surface Dynamics*, *2*, 1–7. https://doi.org/10.5194/esurf-2-1-2014

Segond, M. L., Wheater, H. S., & Onof, C. (2007). The significance of spatial rainfall representation for flood runoff estimation: A numerical evaluation based on the Lee catchment, UK. *Journal of Hydrology*, *347*(1–2), 116–131. https://doi.org/10.1016/j.jhydrol.2007.09.040

Selby, M. J. (1982). Hillslope materials and processes.

Serinaldi, F., Lombardo, F., & Kilsby, C. G. (2020). All in order: Distribution of serially correlated order statistics with applications to hydrological extremes. *Advances in Water Resources*, *144*, 103686. https://doi.org/10.1016/j.advwatres.2020.103686

Sharmeen, S., & Willgoose, G. R. (2006). The interaction between armouring and particle weathering for eroding landscapes. *Earth Surface Processes and Landforms*, *31*(10), 1195–1210. https://doi.org/10.1002/ESP.1397

Sharon, D. (1972). The spottiness of rainfall in a desert area. *Journal of Hydrology*, *17*(3), 161–175. https://doi.org/10.1016/0022-1694(72)90002-9

Sharon, D., & Kutiel, H. (1986). The distribution of rainfall intensity in Israel, its regional and seasonal variations and its climatological evaluation. *Journal of Climatology*, *6*(3), 277–291. https://doi.org/10.1002/joc.3370060304

Sheehan, C. E., & Ward, D. J. (2018). Late Pleistocene talus flatiron formation below the Coal Cliffs cuesta, Utah, USA. *Earth Surface Processes and Landforms*, *43*(9), 1973–1992. https://doi.org/10.1002/esp.4369

Shields, A. (1936). Application of similarity principles and turbulence research to bed-load movement.

Shmilovitz, Y., Enzel, Y., Morin, E., Armon, M., Matmon, A., Mushkin, A., et al. (2022). Aspect-dependent bedrock weathering, cliff retreat, and cliff morphology in a hyperarid environment. *GSA Bulletin*. https://doi.org/10.1130/B36442.1

Shmilovitz, Y., Morin, E., Rinat, Y., Haviv, I., Carmi, G., Mushkin, A., & Enzel, Y. (2020). Linking frequency of rainstorms, runoff generation and sediment transport across hyperarid talus-pediment slopes. *Earth Surface Processes and Landforms*, *45*(7), 1644–1659. https://doi.org/10.1002/esp.4836

Smith, J. A., Baeck, M. L., Yang, L., Signell, J., Morin, E., & Goodrich, D. C. (2019). The Paroxysmal precipitation of the desert: Flash floods in the southwestern United States. *Water Resources Research*, *55*(12), 10218–10247. https://doi.org/10.1029/2019WR025480

Stark, C. P., Barbour, J. R., Hayakawa, Y. S., Hattanji, T., Hovius, N., Chen, H., et al. (2010). The climatic signature of incised river meanders. *Science*, *327*(5972), 1497–1501. https://doi.org/10.1126/science.1184406

Sweeney, K. E., Roering, J. J., & Ellis, C. (2015). Experimental evidence for hillslope control of landscape scale. *Science*, *349*(6243), 51–53. https://doi.org/10.1126/science.aab0017

Thomson, S. N., Brandon, M. T., Tomkin, J. H., Reiners, P. W., Vásquez, C., & Wilson, N. J. (2010). Glaciation as a destructive and constructive control on mountain building. *Nature*, *467*(7313), 313–317. https://doi.org/10.1038/nature09365

Tucker, G. E. (2004). Drainage basin sensitivity to tectonic and climatic forcing: Implications of a stochastic model for the role of entrainment and erosion thresholds. *Earth Surface Processes and Landforms*, *29*(2), 185–205. https://doi.org/10.1002/esp.1020

Tucker, G. E., & Bras, R. L. (2000). A stochastic approach to modeling the role of rainfall variability in drainage basin evolution. *Water Resources Research*, *36*(7), 1953–1964. https://doi.org/10.1029/2000WR900065

Tucker, G. E., & Slingerland, R. (1997). Drainage basin responses to climate change. *Water Resources Research*, *33*(8), 2031–2047. https://doi.org/10.1029/97WR00409

Verdian, J. P., Sklar, L. S., Riebe, C. S., & Moore, J. R. (2021). Sediment size on talus slopes correlates with fracture spacing on bedrock cliffs: Implications for predicting initial sediment size distributions on hillslopes. *Earth Surface Dynamics*, *9*(4), 1073–1090. https://doi.org/10.5194/ESURF-9-1073-2021

Villarini, G., & Krajewski, W. F. (2010). Review of the different sources of uncertainty in single polarization radar-based estimates of rainfall. *Surveys in Geophysics*, *31*(1), 107–129. https://doi.org/10.1007/s10712-009-9079-x

Villarini, G., Mandapaka, P. V., Krajewski, W. F., & Moore, R. J. (2008). Rainfall and sampling uncertainties: A rain gauge perspective. *Journal of Geophysical Research*, *113*(D11), 11102. https://doi.org/10.1029/2007JD009214

Vincendon, B., Ducrocq, V., Nuissier, O., & Vié, B. (2011). Perturbation of convection-permitting NWP forecasts for flash-flood ensemble forecasting. *Natural Hazards and Earth System Sciences*, *11*(5), 1529–1544. https://doi.org/10.5194/NHESS-11-1529-2011

Ward, D. J., Berlin, M. M., & Anderson, R. S. (2011). Sediment dynamics below retreating cliffs. *Earth Surface Processes and Landforms*, *36*(8), 1023–1043. https://doi.org/10.1002/esp.2129

Wilson, P. S., & Toumi, R. (2005). A fundamental probability distribution for heavy rainfall. *Geophysical Research Letters*, *32*(14), L14812. https://doi.org/10.1029/2005gl022465

Wolman, M. G. (1954). A method of sampling coarse river-bed material. *Eos, Transactions American Geophysical Union*, *35*(6), 951–956. https://doi.org/10.1029/TR035I006P00951

Wolman, M. G., & Gerson, R. (1978). Relative scales of time and effectiveness of climate in watershed geomorphology. *Earth Surface Processes*, *3*(2), 189–208. https://doi.org/10.1002/ESP.3290030207/FORMAT/PDF/OEBPS/PAGES/2.PAGE.XHTML

Wolman, M. G., & Miller, J. P. (1960). Magnitude and frequency of forces in geomorphic processes. *The Journal of Geology*, *68*(1), 54–74. https://doi.org/10.1086/626637

Yair, A. (1983). Hillslope hydrology water harvesting and areal distribution of some ancient agricultural systems in the northern Negev desert. *Journal of Arid Environments*, *6*(3), 283–301. https://doi.org/10.1016/S0140-1963(18)31514-3

Yair, A., & Lavee, H. (1985). Runoff generation in arid and semi-arid zones. In *Hydrological forecasting*. MG Anderson and TP Burt.

Yair, A., & Raz-Yassif, N. (2004). Hydrological processes in a small arid catchment: Scale effects of rainfall and slope length. *Geomorphology*, *61*(1–2), 155–169. https://doi.org/10.1016/j.geomorph.2003.12.003

Yakir, H., & Morin, E. (2011). Hydrologic response of a semi-arid watershed to spatial and temporal characteristics of convective rain cells. *Hydrology and Earth System Sciences*, *15*(1), 393–404. https://doi.org/10.5194/hess-15-393-2011

Yokochi, R., Ram, R., Zappala, J. C., Jiang, W., Adar, E., Bernier, R., et al. (2019). Radiokrypton unveils dual moisture sources of a deep desert aquifer. *Proceedings of the National Academy of Sciences of the United States of America*, *116*(33), 16222–16227. https://doi.org/10.1073/pnas.1904260116

Yuter, S. E., & Houze, R. A., Jr. (1995). Three-dimensional kinematic and microphysical evolution of Florida cumulonimbus. Part I: Spatial distribution of updrafts, downdrafts, and precipitation. *Monthly Weather Review*, *123*(7), 1921–1940. https://doi.org/10.1175/1520-0493(1995)123<1921:tdkame>2.0.co;2

yuvalsmilo. (2023). yuvalsmilo/HydroSimStorms: July 20, 2023 Release (1.1.0). *Zenodo*. https://doi.org/10.5281/zenodo.8161362

Zängl, G., Reinert, D., Rípodas, P., & Baldauf, M. (2015). The ICON (ICOsahedral Non-hydrostatic) modelling framework of DWD and MPI-M: Description of the non-hydrostatic dynamical core. *Quarterly Journal of the Royal Meteorological Society*, *141*(687), 563–579. https://doi.org/10.1002/qj.2378

Zhang, P., Molnar, P., & Downs, W. R. (2001). Increased sedimentation rates and grain sizes 2–4 Myr ago due to the influence of climate change on erosion rates. *Nature*, *410p*, 891–897.

Zhang, R. (1997). Determination of soil sorptivity and hydraulic conductivity from the disk infiltrometer. *Soil Science Society of America Journal*, *61*(4), 1024–1030. https://doi.org/10.2136/sssaj1997.03615995006100040005x

Zilberman, E. (2000). Formation of makhteshim unique erosion cirques in the Negev, southern Israel. *Israel Journal of Earth Sciences*, *49*(3), 127–141. https://doi.org/10.1560/8c09-4mj4-ry2p-8k30

Zoccatelli, D., Marra, F., Armon, M., Rinat, Y., Smith, J. A., & Morin, E. (2019). Contrasting rainfall-runoff characteristics of floods in desert and Mediterranean basins. *Hydrology and Earth System Sciences*, *23*(6), 2665–2678. https://doi.org/10.5194/hess-23-2665-2019

Zoccatelli, D., Marra, F., Smith, J., Goodrich, D., Unkrich, C., Rosensaft, M., & Morin, E. (2020). Hydrological modelling in desert areas of the eastern Mediterranean. *Journal of Hydrology*, *587*(February), 124879. https://doi.org/10.1016/j.jhydrol.2020.124879

Zorzetto, E., Botter, G., & Marani, M. (2016). On the emergence of rainfall extremes from ordinary events. *Geophysical Research Letters*, *43*(15), 8076–8082. https://doi.org/10.1002/2016GL069445

References From the Supporting Information

Adams, J. M., Gasparini, N. M., Hobley, D. E. J., Tucker, G. E., Hutton, E. W. H., Nudurupati, S. S., & Istanbulluoglu, E. (2017). The Landlab v1.0 OverlandFlow component: A Python tool for computing shallow-water flow across watersheds. *Geoscientific Model Development*, *10*(4), 1645–1663. https://doi.org/10.5194/gmd-10-1645-2017

Bechtold, P., Köhler, M., Jung, T., Doblas-Reyes, F., Leutbecher, M., Rodwell, M. J., et al. (2008). Advances in simulating atmospheric variability with the ECMWF model: From synoptic to decadal time-scales. *Quarterly Journal of the Royal Meteorological Society*, *134*(634), 1337–1351. https://doi.org/10.1002/qj.289

Brooks, R. H., & Corey, A. T. (1964). *Hydraulic properties of porous media. Hydrology Paper No. 3*. Civil Engineering Department, Colorado State University.

Heber Green, W., & Ampt, G. A. (1911). Studies on soil physics. *The Journal of Agricultural Science*, *4*(1), 1–24. https://doi.org/10.1017/S0021859600001441

Hogan, R. J., & Bozzo, A. (2018). A flexible and efficient radiation scheme for the ECMWF model. *Journal of Advances in Modeling Earth Systems*, *10*(8), 1990–2008. https://doi.org/10.1029/2018MS001364

Khain, P., Levi, Y., Muskatel, H., Shtivelman, A., Vadislavsky, E., & Stav, N. (2021). Effect of shallow convection parametrization on cloud resolving NWP forecasts over the Eastern Mediterranean. *Atmospheric Research*, *247*, 105213. https://doi.org/10.1016/J.ATMOSRES.2020.105213

Raschendorfer, M. (2001). The new turbulence parameterization of LM. *COSMO Newsletter*, *1*, 89–97.

Rawls, W. J., Ahuja, L. R., Brakensiek, D. L., & Shirmohammadi, A. (1992). *Infiltration and soil water movement*. McGraw-Hill Inc.

Rengers, F. K., Tucker, G. E., Moody, J. A., & Ebel, B. A. (2016). Illuminating wildfire erosion and deposition patterns with repeat terrestrial lidar. *Journal of Geophysical Research: Earth Surface*, *121*(3), 588–608. https://doi.org/10.1002/2015JF003600

Schulz, J.-P., & Vogel, G. (2020). Improving the processes in the land surface scheme TERRA: Bare soil evaporation and skin temperature. *Atmosphere*, *11*(5), 513. https://doi.org/10.3390/atmos11050513

Seifert, A. (2008). 3 working group on physical aspects.